An efficient fluid–structure interaction model for optimizing twistable flapping wings

Wang, Qi; Goosen, J. F.L.; van Keulen, F.

DOI
10.1016/j.jfluidstructs.2017.06.006

Publication date
2017

Document Version
Accepted author manuscript

Published in
Journal of Fluids and Structures

Citation (APA)
Wang, Q., Goosen, J. F. L., & van Keulen, F. (2017). An efficient fluid–structure interaction model for optimizing twistable flapping wings. *Journal of Fluids and Structures*, *73*, 82-99. https://doi.org/10.1016/j.jfluidstructs.2017.06.006

Important note
To cite this publication, please use the final published version (if applicable).
Please check the document version above.

Link to formal publication "Journal of Fluids and Structures(Elsevier), Vol. 73, pp 82-99:
https://doi.org/10.1016/j.jfluidstructs.2017.06.006

An Efficient Fluid-Structure Interaction Model for Optimizing Twistable Flapping Wings

Q. Wang*, J.F.L. Goosen, F. van Keulen

Department of Precision and Microsystems Engineering, Structural Optimization and Mechanics Section, Delft University of Technology, Mekelweg 2, Delft, 2628 CD, The Netherlands

Abstract

Spanwise twist can dominate the deformation of flapping wings and alters the aerodynamic performance and power efficiency of flapping wings by changing the local angle of attack. Traditional Fluid-Structure Interaction (FSI) models, based on Computational Structural Dynamics (CSD) and Computational Fluid Dynamics (CFD), have been used to investigate the influence of twist on the power efficiency. However, it is impractical to use them for twist optimization due to the high computational cost. On the other hand, it is of great interest to study the optimal twist of flapping wings. In this work, we propose a computationally efficient FSI model based on an analytical twist model and a quasi-steady aerodynamic model which replace the expensive CSD and CFD methods. The twist model uses a polynomial to describe the change of the twist angle along the span. The polynomial order is determined based on a convergence study. A nonlinear plate model is used to evaluate the structural response of the twisted wing. The adopted quasi-steady aerodynamic model analytically calculates the aerodynamic loads by including four loading terms which originate from the wing's translation, rotation, their coupling and the added-mass effect. Based on the proposed FSI model, we optimize the twist of a rectangular wing by minimizing the power consumption during hovering flight. The power efficiency of optimized twistable and rigid wings is studied. Comparisons indicates that the optimized twistable wings exhibit power efficiencies close to the optimized rigid wings, unless the pitching amplitude at the wing root is limited. When the pitching amplitude at the root decreases by increasing the root stiffness, the optimized rigid wings need more power for hovering. However, with the help of wing twist, the power efficiencies of optimized twistable wings with a prescribed root stiffness are comparable with the twistable wings with an optimal root stiffness. This observation provides an explanation for the different levels of twist exhibited by insect wings. The high computational efficiency of the proposed FSI model allows further application to parametric studies and optimization of flapping wings. This will enhance the understanding of insect wing flexibility and help the design of flexible artificial wings for flapping wing micro air vehicles.

Keywords: twistable flapping wing, fluid-structure interaction, hovering flight, power efficiency, optimization

*Corresponding author
Email addresses: Q.Wang-3@tudelft.nl (Q. Wang), J.F.L.Goosen@tudelft.nl (J.F.L. Goosen), A.vanKeulen@tudelft.nl (F. van Keulen)

1. Introduction

Flapping wings keep receiving attention from biologists and engineers due to the increasing interest in flapping wing micro air vehicles (FWMAVs). Inspired by insect wings, the kinematics and shape for FWMAV wings have been studied more extensively as compared to the wing flexibility.

The wing thickness is typically one to two orders smaller than the wing span and, consequently, insects wings can be modeled as thin-walled structures. The apparent wing flexibility depends on the morphological characteristics, e.g., the venation layout, cross-sectional profile and the membrane thickness. Due to the inertial and aerodynamic loads, dramatic out-of-plane deformation can be observed for some insect wings. The deformation can be decomposed into three modes (Wootton, 1981): spanwise bending, spanwise twist and chordwise camber. For insect wings, the deformation can be dominated by different modes (Willmott and Ellington, 1997a; Chen *et al.*, 2013; Zheng *et al.*, 2013).

For artificial wings, the deformation can also be described by the three modes. Among them, the twist is of particular interest for realizing power-efficient wing designs because of four reasons. First, to realize the required wing kinematics, the spanwise bending is normally restricted by the wing structural designs, e.g., using longitudinal stiffeners (Bolsman *et al.*, 2009; de Croon *et al.*, 2009; Nan *et al.*, 2017) or chordwise corrugations (Tanaka and Wood, 2010; Tanaka, 2012). Second, the turbulent flow surrounding flapping wings is not as sensitive as a laminar flow to the wing camber (Du and Sun, 2010). Third, cm-scale flapping wings (Bolsman *et al.*, 2009; Deng *et al.*, 2016; Nan *et al.*, 2017) are commonly used for FWMAVs. Such wings can exhibit large twist due to the large difference of the inertial and aerodynamic loads at the wing root and tip. Fourth, the twist can dramatically alter the local angle of attack along the span, which changes the aerodynamic performance and the power efficiency. Therefore, this work exclusively focuses on the modeling and effects of wing twist. In addition, only hovering flight is considered because (1) the wing deformation is most pronounced during hovering flight (Willmott and Ellington, 1997a), and (2) hovering flight is generally more power-consuming as compared to forward flight (Dudley, 2002).

Traditional Fluid-Structure Interaction (FSI) models, based on Computational Structural Dynamics (CSD) and Computational Fluid Dynamics (CFD), have been used to investigate the influence of wing twist on the aerodynamic performance and power efficiency of different flapping wings. For example, Du and Sun (2008) studied the effects of unsteady deformation of flapping wings on the aerodynamic force production and power consumption. They showed that lift is increased by up to 20% and lift-to-drag ratio by around 10% with a deformation of 6% camber and 20° twist when compared with the rigid counterparts. Meanwhile, the power required is reduced by about 16%. Shyy *et al.* (2010) showed that wing twist can make FWMAVs more susceptible to gusty conditions. Nakata and Liu (2012a) performed a FSI analysis of hawkmoth hovering with flexible wings through an integrated wing-body modeling of the morphology, kinematics and flexibility. Their results demonstrate the importance of inherent flexibility of insect wing in enhancing aerodynamic performance during flapping flight. Dai *et al.* (2012) conducted three-dimensional FSI simulation of a low aspect-ratio rectangular wing performing a hovering flight. They observed that the twist disappears somewhere between the wing reversal and mid-stroke. More recently, Nguyen and Han (2016) showed that the effects of the FSI are the most significant in hovering flight of an hawkmoth wing and tend to decrease with the forward flight speed. However, limited by the high computational cost, it is impractical to use traditional FSI models for twist optimization. The latter is of great interest for the study of insect wings and the design of ar-

tificial wings. There are some analytical models which capture the FSI effect to some levels. For instance, Calogero *et al.* (2016) modeled the compliant joints as spherical joints with distributed mass and spring-dampers with coupled nonlinear spring and damping coefficients, which greatly reduces computational time as compared to the CSD analysis. However, the realistic aerodynamic loads have not been included in their simulation yet. Moreover, most of the studies on FSI of flexible wings prescribed the pitching motion at the root, while in reality passive pitching is widely used by wings of insects (Ennos, 1989; Bergou *et al.*, 2007) and FWMAVs (de Croon *et al.*, 2009; Bolsman *et al.*, 2009; Dai *et al.*, 2012; Ma *et al.*, 2013). The prescribed pitching motion helps the simulation to converge easier and reduces the computational cost. However, the power consumption of flapping wings with prescribed and passive pitching motion can differ dramatically (Han *et al.*, 2015). In this work, we propose a computationally efficient FSI model to study the (optimal) twist of flapping wings. The proposed FSI model uses an analytical twist model for the structural analysis and a quasi-steady aerodynamic model (Wang *et al.*, 2016) for the aerodynamic analysis.

This paper is structured as follows. The modeling of twistable flapping wings and the FSI is presented in Sec. 2. In Sec. 3, the proposed twist model is validated. In Sec. 4, flapping wing twist and kinematics are optimized by minimizing the power consumption for hovering using the proposed FSI model. Conclusions are presented in Sec. 5.

2. Modeling of twistable flapping wings

In this work, rectangular flapping wings with uniform thickness are studied. The wings will be modeled as isotropic and homogeneous plates which exhibit twist. Linear elastic material model will be used for structural analysis. In the following subsections, the wing kinematic model and equations of motion will be introduced.

2.1. Kinematics

The wing motion can be described by a combination of three successive rigid-body rotations and an elastic deformation, as illustrated in Fig. 1. The rigid-body rotations consist of the sweeping motion about the z_i axis of the inertial frame $x_\mathrm{i}y_\mathrm{i}z_\mathrm{i}$, the heaving motion about the y_θ axis of the intermediate frame $x_\theta y_\theta z_\theta$, and the pitching motion about the y_η axis of another intermediate frame $x_\eta y_\eta z_\eta$. Thereafter, the frame $x_\mathrm{c}y_\mathrm{c}z_\mathrm{c}$ which co-rotates with the undeformed wing is introduced. The co-rotating frame has its x_c axis directing from the root to the tip of the undeformed wing. Its z_c axis coincides with the undeformed wing plane. Three Euler angles, namely the sweeping angle ϕ, heaving angle θ and the pitching angle η, are used to quantify these rotations. The corresponding rotation matrices are

$$\boldsymbol{R}_\phi = \begin{bmatrix} \cos\phi & -\sin\phi & 0 \\ \sin\phi & \cos\phi & 0 \\ 0 & 0 & 1 \end{bmatrix}, \quad \boldsymbol{R}_\theta = \begin{bmatrix} \cos\theta & 0 & \sin\theta \\ 0 & 1 & 0 \\ -\sin\theta & 0 & \cos\theta \end{bmatrix} \quad \text{and} \quad \boldsymbol{R}_\eta = \begin{bmatrix} 1 & 0 & 0 \\ 0 & \cos\eta & -\sin\eta \\ 0 & \sin\eta & \cos\eta \end{bmatrix}. \tag{1}$$

The wing's elastic deformation is defined with respect to the co-rotating frame in order to decouple wing deformation and finite rigid-body motions. For a general point P at the mid-plane of the twisted wing, as shown in Fig. 2, the position vector is denoted as $\boldsymbol{r}_\mathrm{i} = [x_\mathrm{i}, y_\mathrm{i}, z_\mathrm{i}]^\mathrm{T}$ in the inertial frame or $\boldsymbol{r}_\mathrm{c} = [x_\mathrm{c}, y_\mathrm{c}, z_\mathrm{c}]^\mathrm{T}$ in the co-rotating frame. In the co-rotating frame, the position vector $\boldsymbol{r}_\mathrm{i}$ is related to $\boldsymbol{r}_\mathrm{c}$ via the transformation matrix $\boldsymbol{R}_{\mathrm{c}\to\mathrm{i}}$ ($= \boldsymbol{R}_\phi\boldsymbol{R}_\theta\boldsymbol{R}_\eta$). $\boldsymbol{r}_\mathrm{c}$ can be decomposed as

$$\boldsymbol{r}_\mathrm{c} = \boldsymbol{r}_{\mathrm{c}0} + \boldsymbol{r}_\mathrm{c}^\mathrm{ela}, \tag{2}$$

where $\boldsymbol{r}_{c0}$ ($=[x_{c0}, 0, z_{c0}]^T$) is the position vector of point P before twist, and $\boldsymbol{r}_c^{ela}$ ($=[u_{x_c}, u_{y_c}, u_{z_c}]^T$) is the corresponding elastic displacement. The components u_{x_c}, u_{y_c} and u_{z_c} represent the displacement in the x_c, y_c and z_c directions, respectively, as shown in Fig. 2. Two assumptions are made regarding wing twist. First, an arbitrary chord from the untwisted wing stays straight and unstretched after twist. Second, the spanwise displacement due to the shortening effect (Trahair,

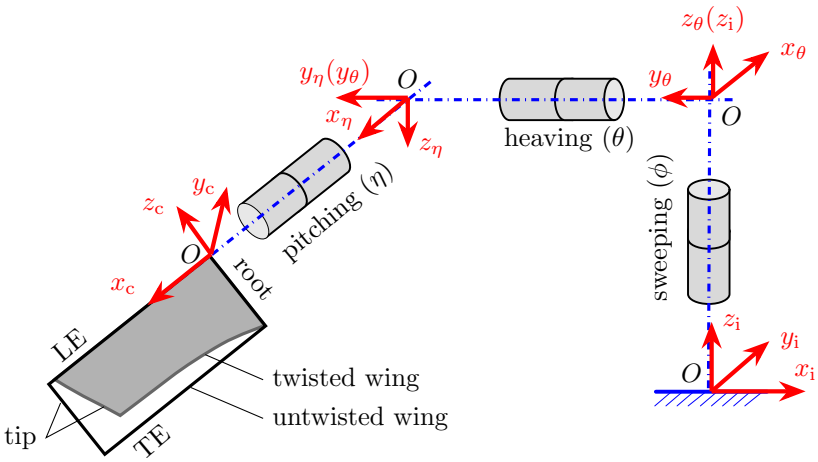

Figure 1: Schematic diagram of a twisted rectangular flapping wing. Three successive rigid-body rotations corresponding to the sweeping, heaving and pitching motion are illustrated using the "cans in series" approach (Schwab and Meijaard, 2006). Four frames are involved in the rigid-body rotations, including the inertial frame $x_i y_i z_i$, two intermediate frames $x_\theta y_\theta z_\theta$ and $x_\eta y_\eta z_\eta$, and the co-rotating frame $x_c y_c z_c$. These frames share the same origin O.

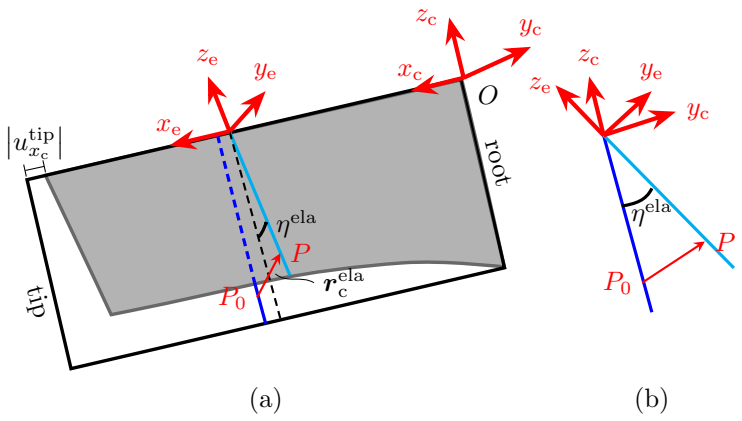

Figure 2: Schematic diagram of the elastic displacement of a twisted rectangular wing. The elastic frame $x_e y_e z_e$ is generated by first translating the co-rotating frame $x_c y_c z_c$ along the leading edge and then rotating by the local twist angle. P_0 and P indicate the positions of an arbitrary point at the mid-plane before and after twist. The spanwise tip displacement and the local pitching angle are denoted as $u_{x_c}^{tip}$ and η^{ela}, respectively. $u_{x_c}^{tip}$ will be negative due to the shortening effect. (a) 3D view of the untwisted and twisted wing. (b) 2D view of the local chord when observed from the wing tip.

2005) changes linearly from zero at the wing root to $u_{x_c}^{\text{tip}}$ (< 0) at the tip. Thus, the displacement of point P can be given by

$$\boldsymbol{r}_{\text{c}}^{\text{ela}} = \begin{bmatrix} u_{x_c} \\ u_{y_c} \\ u_{z_c} \end{bmatrix} = \begin{bmatrix} u_{x_c}^{\text{tip}} x_{\text{c0}}/R \\ -z_{\text{c0}} \sin(\eta^{\text{ela}}) \\ z_{\text{c0}}[\cos(\eta^{\text{ela}}) - 1] \end{bmatrix}. \tag{3}$$

Here R is the span of the undeformed wing, and η^{ela} is the local, additional, pitching angle induced by twist. A polynomial function of degree n is used to approximate the change of η^{ela} along the span, i.e.,

$$\eta^{\text{ela}} = \sum_{i=1}^{n} a_i x_{\text{c0}}^i, \qquad 0 \leqslant x_{\text{c0}} \leqslant R, \tag{4}$$

where the coefficients a_i, $i \in [1, ..., n]$, are determined by the twist angles at n different locations. For convenience, the chords with $x_{\text{c0}} = iR/n$ are selected, and the corresponding twist angles are denoted by q_i^{ela}. Thus, the polynomial coefficients of Eq. 4 are determined by

$$\begin{bmatrix} a_1 \\ a_2 \\ \vdots \\ a_n \end{bmatrix} = \begin{bmatrix} R/n & (R/n)^2 & \dots & (R/n)^n \\ 2R/n & (2R/n)^2 & \dots & (2R/n)^n \\ \vdots & \vdots & \ddots & \vdots \\ nR/n & (nR/n)^2 & \dots & (nR/n)^n \end{bmatrix}^{-1} \begin{bmatrix} q_1^{\text{ela}} \\ q_2^{\text{ela}} \\ \vdots \\ q_n^{\text{ela}} \end{bmatrix}. \tag{5}$$

As shown in Fig. 2, the elastic frame $x_{\text{e}}y_{\text{e}}z_{\text{e}}$ is committed to a local chord. This frame is generated by first translating the co-rotating frame $x_{\text{c}}y_{\text{c}}z_{\text{c}}$ along the leading edge and then rotating it by the local twist angle. In this frame, the translational velocity and acceleration of the chord can be calculated by

$$\boldsymbol{v}_{\text{e}} = \left[v_{x_{\text{e}}}, v_{y_{\text{e}}}, v_{z_{\text{e}}}\right]^{\text{T}} = \boldsymbol{R}_{\text{e}\to\text{i}}^{\text{T}} \dot{\boldsymbol{R}}_{\text{e}\to\text{i}} [x_{\text{e}}, 0, 0]^{\text{T}} \tag{6}$$

and

$$\boldsymbol{a}_{\text{e}} = \left[a_{x_{\text{e}}}, a_{y_{\text{e}}}, a_{z_{\text{e}}}\right]^{\text{T}} = \boldsymbol{R}_{\text{e}\to\text{i}}^{\text{T}} \ddot{\boldsymbol{R}}_{\text{e}\to\text{i}} [x_{\text{e}}, 0, 0]^{\text{T}}, \tag{7}$$

respectively, where $\boldsymbol{R}_{\text{e}\to\text{i}}$ ($=\boldsymbol{R}_\phi \boldsymbol{R}_\theta \boldsymbol{R}_\eta \boldsymbol{R}_{\text{e}}$) is the resulting transformation matrix from the elastic frame to the inertial frame. The rotational velocity and acceleration of the chord can be obtained by

$$\boldsymbol{\omega}_{\text{e}} = \left[\omega_{x_{\text{e}}}, \omega_{y_{\text{e}}}, \omega_{z_{\text{e}}}\right]^{\text{T}} = \boldsymbol{R}_{\text{e}\to\text{i}}^{\text{T}} \left[0, 0, \dot{\phi}\right]^{\text{T}} + \boldsymbol{R}_{\text{e}\to\theta}^{\text{T}} \left[0, \dot{\theta}, 0\right]^{\text{T}} + \left[\dot{\eta} + \dot{\eta}^{\text{ela}}, 0, 0\right]^{\text{T}} \tag{8}$$

and

$$\boldsymbol{\alpha}_{\text{e}} = \left[\alpha_{x_{\text{e}}}, \alpha_{y_{\text{e}}}, \alpha_{z_{\text{e}}}\right]^{\text{T}} = \boldsymbol{R}_{\text{e}\to\text{i}}^{\text{T}} \left[0, 0, \ddot{\phi}\right]^{\text{T}} + \boldsymbol{R}_{\text{e}\to\theta}^{\text{T}} \left[0, \ddot{\theta}, 0\right]^{\text{T}} + \left[\ddot{\eta} + \ddot{\eta}^{\text{ela}}, 0, 0\right]^{\text{T}}, \tag{9}$$

respectively, with $\boldsymbol{R}_{\text{e}\to\theta}$ ($=\boldsymbol{R}_\theta \boldsymbol{R}_\eta \boldsymbol{R}_{\text{e}}$) representing the resulting transformation matrix from the elastic frame to the frame $x_\theta y_\theta z_\theta$. These translational and rotational quantities will be used for the calculation of aerodynamic forces and power consumption of twistable wings.

2.2. Equations of motion

The generalized coordinates that determine the wing kinematics include

$$\boldsymbol{q} = \left[\left[\boldsymbol{q}^{\text{rot}}\right]^{\text{T}}, \left[\boldsymbol{q}^{\text{ela}}\right]^{\text{T}}\right]^{\text{T}}, \tag{10}$$

where $\boldsymbol{q}^{\mathrm{rot}}$ (= $[q_1^{\mathrm{rot}}, q_2^{\mathrm{rot}}, q_3^{\mathrm{rot}}]^{\mathrm{T}}$) and $\boldsymbol{q}^{\mathrm{ela}}$ (= $[q_1^{\mathrm{ela}}, q_2^{\mathrm{ela}}, ..., q_n^{\mathrm{ela}}, q_{n+1}^{\mathrm{ela}}]^{\mathrm{T}}$) are associated to the wing rigid-body rotations and the elastic deformation, respectively. For convenience, $\boldsymbol{q}^{\mathrm{rot}}$ and $\boldsymbol{q}^{\mathrm{ela}}$ will be referred to as rotational and elastic generalized coordinates, respectively. The first n coordinates of $\boldsymbol{q}^{\mathrm{ela}}$ have been introduced in Eq. 5. The coordinates q_1^{rot}, q_2^{rot}, q_3^{rot} and q_{n+1}^{ela} represent the sweeping angle ϕ, heaving angle θ, pitching angle η and the spanwise tip displacement $u_{x_{\mathrm{c}}}^{\mathrm{tip}}$, respectively.

The wing's equations of motion can be derived from Lagrange's equation

$$\frac{d}{dt}\left(\frac{\partial E_{\mathrm{k}}}{\partial \dot{\boldsymbol{q}}}\right) - \frac{\partial E_{\mathrm{k}}}{\partial \boldsymbol{q}} + \frac{\partial E_{\mathrm{p}}}{\partial \boldsymbol{q}} = \boldsymbol{Q}^{\mathrm{ext}}, \tag{11}$$

with E_{k} and E_{p} representing the wing's kinetic and potential energy, respectively, and $\boldsymbol{Q}^{\mathrm{ext}}$ the generalized forces related to the external drive and aerodynamic loads.

2.2.1. Kinetic energy

The wing's kinetic energy can be calculated by

$$E_{\mathrm{k}} = \frac{1}{2}\iint_S h\rho^{\mathrm{w}} \dot{\boldsymbol{r}}_{\mathrm{i}}^{\mathrm{T}} \dot{\boldsymbol{r}}_{\mathrm{i}} ds = \frac{1}{2}\iint_S h\rho^{\mathrm{w}} \left(\boldsymbol{L}\dot{\boldsymbol{q}}\right)^{\mathrm{T}} \boldsymbol{L}\dot{\boldsymbol{q}} ds \triangleq \frac{1}{2}\dot{\boldsymbol{q}}^{\mathrm{T}} \boldsymbol{M}^{\mathrm{w}} \dot{\boldsymbol{q}}, \tag{12}$$

where h is the wing thickness, S is the area of the untwisted wing, ρ^{w} is the wing density, and $\boldsymbol{M}^{\mathrm{w}}$ is the wing's mass matrix. $\boldsymbol{M}^{\mathrm{w}}$ is given by

$$\boldsymbol{M}^{\mathrm{w}} = \iint_S h\rho^{\mathrm{w}} \boldsymbol{L}^{\mathrm{T}} \boldsymbol{L} ds, \tag{13}$$

with

$$\boldsymbol{L} = \left[\frac{\partial\left(\boldsymbol{R}_{\mathrm{c}\to\mathrm{i}}\boldsymbol{r}_{\mathrm{c}}\right)}{\partial \boldsymbol{q}^{\mathrm{rot}}}, \boldsymbol{R}_{\mathrm{c}\to\mathrm{i}}\frac{\partial \boldsymbol{r}_{\mathrm{c}}}{\partial \boldsymbol{q}^{\mathrm{ela}}}\right]. \tag{14}$$

Substituting the kinetic energy (Eq. 12) into the first two terms at the left-hand side of the Lagrange's equation (Eq. 11) yields

$$\frac{d}{dt}\left(\frac{\partial E_{\mathrm{k}}}{\partial \dot{\boldsymbol{q}}}\right) - \frac{\partial E_{\mathrm{k}}}{\partial \boldsymbol{q}} = \boldsymbol{M}^{\mathrm{w}}\ddot{\boldsymbol{q}} + \boldsymbol{Q}_{\mathrm{v}}, \tag{15}$$

where $\boldsymbol{Q}_{\mathrm{v}}$ represents the sum of the centrifugal and Coriolis forces, i.e.,

$$\boldsymbol{Q}_{\mathrm{v}} = \dot{\boldsymbol{M}}^{\mathrm{w}}\dot{\boldsymbol{q}} - \left[\frac{\partial}{\partial \boldsymbol{q}}\left(\frac{1}{2}\dot{\boldsymbol{q}}^{\mathrm{T}}\boldsymbol{M}^{\mathrm{w}}\dot{\boldsymbol{q}}\right)\right]^{\mathrm{T}}. \tag{16}$$

2.2.2. Elastic potential energy

Typically, the pitching motion of flapping wings results from both the torsion/bending of the elastic elements at the wing root (e.g., torsional spring, elastic hinge or slender beam) and the deformation of the wing plate. These two contributions are functions of the generalized coordinates $\boldsymbol{q}^{\mathrm{rot}}$ and $\boldsymbol{q}^{\mathrm{ela}}$, respectively. Therefore, the total wing potential energy can be decomposed into

$$E_{\mathrm{p}} = E_{\mathrm{p}}^{\mathrm{rot}}\left(\boldsymbol{q}^{\mathrm{rot}}\right) + E_{\mathrm{p}}^{\mathrm{ela}}\left(\boldsymbol{q}^{\mathrm{ela}}\right), \tag{17}$$

with $E_{\mathrm{p}}^{\mathrm{rot}}$ and $E_{\mathrm{p}}^{\mathrm{ela}}$ representing the elastic energy related to the rigid-body rotations and the elastic wing twist, respectively. By assuming linear elastic root elements (Howell, 2001; Whitney and Wood, 2010; Wang *et al.*, 2014), $E_{\mathrm{p}}^{\mathrm{rot}}$ can be formulated as

$$E_{\mathrm{p}}^{\mathrm{rot}} = \frac{1}{2}\left[\boldsymbol{q}^{\mathrm{rot}}\right]^{\mathrm{T}} \boldsymbol{K}^{\mathrm{rot}} \boldsymbol{q}^{\mathrm{rot}}, \tag{18}$$

where $\boldsymbol{K}^{\mathrm{rot}}$ represents the stiffness matrix associated to the rigid-body rotations. Based on the linear elastic material model, the potential energy $E_{\mathrm{p}}^{\mathrm{ela}}$ can be calculated by

$$E_{\mathrm{p}}^{\mathrm{ela}} = \frac{1}{2}\iiint_{V} \boldsymbol{\epsilon}^{T} \boldsymbol{C} \boldsymbol{\epsilon} dv, \tag{19}$$

of which V is the wing volume, $\boldsymbol{\epsilon}$ is the wing strain, and $\boldsymbol{C}$ is the matrix with elastic coefficients. Nonlinear strain-displacement relations for plates with moderate deformation are used to calculate the strain, as given by

$$\boldsymbol{\epsilon} = \begin{bmatrix} \epsilon_{x_{\mathrm{c}}0} \\ \epsilon_{z_{\mathrm{c}}0} \\ \gamma_{x_{\mathrm{c}}0 z_{\mathrm{c}}0} \end{bmatrix} = \begin{bmatrix} \frac{\partial u_{x_{\mathrm{c}}}}{\partial x_{\mathrm{c}}} + \frac{1}{2}\left(\frac{\partial u_{x_{\mathrm{c}}}}{\partial x_{\mathrm{c}}}\right)^2 + \frac{1}{2}\left(\frac{\partial u_{z_{\mathrm{c}}}}{\partial x_{\mathrm{c}}}\right)^2 + \frac{1}{2}\left(\frac{\partial u_{y_{\mathrm{c}}}}{\partial x_{\mathrm{c}}}\right)^2 - y_{\mathrm{c}}\frac{\partial^2 u_{y_{\mathrm{c}}}}{\partial x_{\mathrm{c}}^2} \\ \frac{\partial u_{z_{\mathrm{c}}}}{\partial z_{\mathrm{c}}} + \frac{1}{2}\left(\frac{\partial u_{x_{\mathrm{c}}}}{\partial z_{\mathrm{c}}}\right)^2 + \frac{1}{2}\left(\frac{\partial u_{z_{\mathrm{c}}}}{\partial z_{\mathrm{c}}}\right)^2 + \frac{1}{2}\left(\frac{\partial u_{y_{\mathrm{c}}}}{\partial z_{\mathrm{c}}}\right)^2 - y_{\mathrm{c}}\frac{\partial^2 u_{y_{\mathrm{c}}}}{\partial z_{\mathrm{c}}^2} \\ \frac{\partial u_{z_{\mathrm{c}}}}{\partial x_{\mathrm{c}}} + \frac{\partial u_{x_{\mathrm{c}}}}{\partial z_{\mathrm{c}}} + \frac{\partial u_{x_{\mathrm{c}}}}{\partial z_{\mathrm{c}}}\frac{\partial u_{x_{\mathrm{c}}}}{\partial x_{\mathrm{c}}} + \frac{\partial u_{z_{\mathrm{c}}}}{\partial z_{\mathrm{c}}}\frac{\partial u_{z_{\mathrm{c}}}}{\partial x_{\mathrm{c}}} + \frac{\partial u_{y_{\mathrm{c}}}}{\partial z_{\mathrm{c}}}\frac{\partial u_{y_{\mathrm{c}}}}{\partial x_{\mathrm{c}}} - 2y_{\mathrm{c}}\frac{\partial^2 u_{y_{\mathrm{c}}}}{\partial x_{\mathrm{c}} \partial z_{\mathrm{c}}} \end{bmatrix}, \tag{20}$$

where ϵ and γ represent the normal and shear strain, respectively. It can be observed that Kirchhoff's hypothesis is used and quadratic membrane strain terms are included. The importance of these nonlinear strain terms increases with the twist angle. The constitutive matrix in Eq. 19 is given by

$$\boldsymbol{C} = \frac{E}{1-\nu^2}\begin{bmatrix} 1 & \nu & 0 \\ \nu & 1 & 0 \\ 0 & 0 & (1-\nu)/2 \end{bmatrix}, \tag{21}$$

with E and ν representing the Young's modulus and Poisson's ratio of the wing, respectively.

Knowing $E_{\mathrm{p}}^{\mathrm{rot}}$ and $E_{\mathrm{p}}^{\mathrm{ela}}$, $\frac{\partial E_{\mathrm{p}}}{\partial \boldsymbol{q}}$ can be calculated. The derivative physically represents the generalized elastic force. If the generalized elastic force is denoted as $\boldsymbol{Q}^{\mathrm{ela}}$, we get

$$\frac{\partial E_{\mathrm{p}}}{\partial \boldsymbol{q}} = \boldsymbol{Q}^{\mathrm{ela}}. \tag{22}$$

2.2.3. External forces

The generalized external force in the Lagrange's equation originates from two sources, i.e.,

$$\boldsymbol{Q}^{\mathrm{ext}} = \boldsymbol{Q}^{\mathrm{drive}} + \boldsymbol{Q}^{\mathrm{aero}}, \tag{23}$$

where $\boldsymbol{Q}^{\mathrm{drive}}$ and $\boldsymbol{Q}^{\mathrm{aero}}$ correspond to the drive and aerodynamic loads, respectively. In this work, we assume the drive load to be applied at the wing joint. Therefore, $\boldsymbol{Q}^{\mathrm{drive}}$ can be expressed as

$$\boldsymbol{Q}^{\mathrm{drive}} = [Q_{q_1^{\mathrm{rot}}}^{\mathrm{drive}}, Q_{q_2^{\mathrm{rot}}}^{\mathrm{drive}}, Q_{q_3^{\mathrm{rot}}}^{\mathrm{drive}}, \mathbf{0}_{1\times(n+1)}^{\mathrm{T}}]^{\mathrm{T}}, \tag{24}$$

of which $Q_{q_1^{\mathrm{rot}}}^{\mathrm{drive}}$, $Q_{q_2^{\mathrm{rot}}}^{\mathrm{drive}}$ and $Q_{q_3^{\mathrm{rot}}}^{\mathrm{drive}}$ represent the drive loads applied on the rotational axes corresponding to the sweeping motion, heaving motion and the pitching motion, respectively. Some of

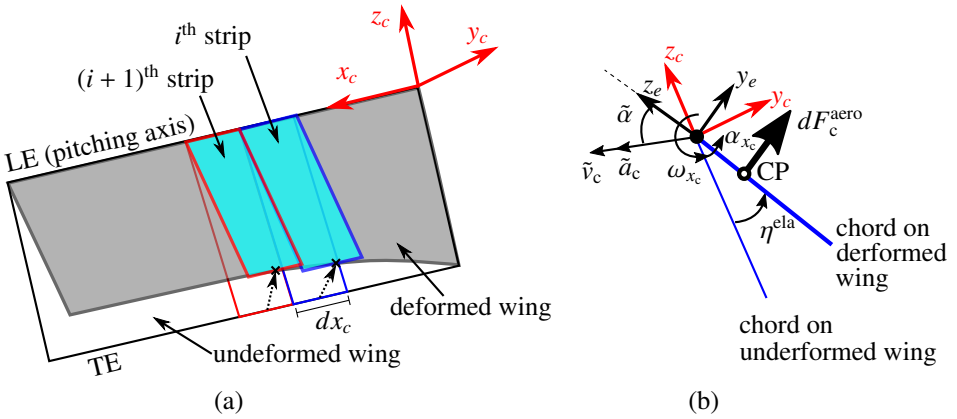

Figure 3: Schematic diagram of the blade element method used with the quasi-steady aerodynamic model. (a) 3D view of a wing configuration with two adjacent chordwise strips before and after twist. The width is exaggerated. (b) 2D side-view of the i^{th} strip. The solid and open circles represent the leading edge and the center of pressure, respectively.

these three terms will be equal to zero if the corresponding motion is fully passive. For instance, $Q^{\text{drive}}_{q_3^{\text{rot}}}$ is zero for wings using passive pitching (Bolsman *et al.*, 2009; Ma *et al.*, 2013).

The generalized aerodynamic force $\boldsymbol{Q}^{\text{aero}}$ is calculated by the quasi-steady aerodynamic model proposed by Wang *et al.* (2016). This model assumes that the transient resultant aerodynamic force $\boldsymbol{F}_{\text{e}}^{\text{aero}}$ does not rely on the flow history and is determined by the transient velocity, acceleration and angle of attack. Due to the wing rotation and twist, the kinematics varies from the wing root to the tip and from the leading edge (LE) to the trailing edge (TE). Therefore, the blade element method (Osborne, 1951) is applied to divide the wing planform into chordwise strips with an infinitesimal width dx_{c}. The infinitesimal resultant aerodynamic force $d\boldsymbol{F}_{\text{e}}^{\text{aero}}$ acting on an arbitrary infinitesimal strip of a twisted wing is approximated by the force on a flat strip. As illustrated in Fig. 3, the flat strip is obtained by rotating the respective strip of the untwisted wing by the local twist angle. The tip displacement $u_{x_{\text{c}}}^{\text{tip}}$ due to the shortening effect is typically two orders smaller than the original span for a moderately twisted wing. Therefore, the change of the wing span due to the twist is neglected for the aerodynamic analysis. The quasi-steady aerodynamic model assumes the resultant force to be perpendicular to the local flat strip considering the pressure load dominates the aerodynamic load on flapping wings (Wang *et al.*, 2016). Therefore, $d\boldsymbol{F}_{\text{e}}^{\text{aero}}$ can be expressed as

$$d\boldsymbol{F}_{\text{e}}^{\text{aero}} = dF_{y_{\text{e}}}^{\text{aero}} \boldsymbol{e}_{y_{\text{e}}}, \tag{25}$$

with $\boldsymbol{e}_{y_{\text{e}}}$ denoting the unit vector in the direction of the y_{e} axis of the elastic frame. The quasi-steady model calculates the magnitude of $dF_{y_{\text{e}}}^{\text{aero}}$ by including four loading terms:

$$dF_{y_{\text{e}}}^{\text{aero}} = \left(\tilde{F}_{y_{\text{e}}}^{\text{trans}} + \tilde{F}_{y_{\text{e}}}^{\text{rot}} + \tilde{F}_{y_{\text{e}}}^{\text{coupl}} + \tilde{F}_{y_{\text{e}}}^{\text{am}}\right) dx_{\text{e}}, \tag{26}$$

where $\tilde{F}_{y_{\text{e}}}^{\text{trans}}$, $\tilde{F}_{y_{\text{e}}}^{\text{rot}}$, $\tilde{F}_{y_{\text{e}}}^{\text{coupl}}$ and $\tilde{F}_{y_{\text{e}}}^{\text{am}}$ represent the force components resulting from the translation, rotation, their coupling and the added-mass effect of a strip of unit width, respectively. The detailed expressions of these forces are provided in Appendix A. The generalized aerodynamic

force for the entire wing can be obtained by

$$\boldsymbol{Q}^{\text{aero}} = \int_0^R \left\{ \tilde{F}^{\text{trans}}_{y_\text{e}} \left[\frac{\partial \boldsymbol{r}^{\text{trans}}_{\text{i,cp}}}{\partial \boldsymbol{q}} \right]^{\text{T}} + \tilde{F}^{\text{rot}}_{y_\text{e}} \left[\frac{\partial \boldsymbol{r}^{\text{rot}}_{\text{i,cp}}}{\partial \boldsymbol{q}} \right]^{\text{T}} + \tilde{F}^{\text{coupl}}_{y_\text{e}} \left[\frac{\partial \boldsymbol{r}^{\text{coupl}}_{\text{i,cp}}}{\partial \boldsymbol{q}} \right]^{\text{T}} + \tilde{F}^{\text{am}}_{y_\text{e}} \left[\frac{\partial \boldsymbol{r}^{\text{am}}_{\text{i,cp}}}{\partial \boldsymbol{q}} \right]^{\text{T}} \right\} \boldsymbol{R}_{\text{e}\to\text{i}} \boldsymbol{e}_{y_\text{e}} dx_\text{e}, \tag{27}$$

with $\boldsymbol{r}^{\text{trans}}_{\text{i,cp}}$, $\boldsymbol{r}^{\text{rot}}_{\text{i,cp}}$, $\boldsymbol{r}^{\text{coupl}}_{\text{i,cp}}$ and $\boldsymbol{r}^{\text{am}}_{\text{i,cp}}$ representing the position vectors of the centers of pressure in the inertial frame. These vectors can be obtained by

$$\boldsymbol{r}^{\oplus}_{\text{i,cp}} = \boldsymbol{R}_{\text{e}\to\text{i}} [x_\text{e}, 0, -c\hat{d}^{\oplus}_{\text{cp}}]^{\text{T}}, \tag{28}$$

with the superscript "$\oplus$" referring to "trans", "rot", "coupl" or "am" for the different loading terms. The locations of the centers of pressure $\hat{d}^{\text{trans}}_{\text{cp}}$, $\hat{d}^{\text{rot}}_{\text{cp}}$, $\hat{d}^{\text{coupl}}_{\text{cp}}$ and $\hat{d}^{\text{am}}_{\text{cp}}$ are also provided in Appendix A.

The first three components of $\boldsymbol{Q}^{\text{aero}}$ are functions of the generalized velocities, but the last term (i.e., the added-mass term) can be separated into two parts which are functions of the generalized velocities and accelerations, respectively. Therefore, $\boldsymbol{Q}^{\text{aero}}$ can be rewritten as

$$\boldsymbol{Q}^{\text{aero}} = \tilde{\boldsymbol{Q}}^{\text{aero}} - \boldsymbol{M}^{\text{am}} \ddot{\boldsymbol{q}}. \tag{29}$$

Here, $\tilde{\boldsymbol{Q}}^{\text{aero}}$ includes all the generalized velocity related terms, and $\boldsymbol{M}^{\text{am}}$ is the mass matrix related to the added-mass effect.

Substituting Eqs. 15, 22, 23 and 29 into the Lagrange's equation in Eq. 11, we can obtain the equations of motion for a twistable wing as in

$$\boldsymbol{M}\ddot{\boldsymbol{q}} = -\boldsymbol{Q}^{\text{ela}} + \boldsymbol{Q}^{\text{drive}} + \tilde{\boldsymbol{Q}}^{\text{aero}} - \boldsymbol{Q}_\text{v}, \tag{30}$$

where $\boldsymbol{M}(= \boldsymbol{M}^{\text{w}} + \boldsymbol{M}^{\text{am}})$ is the effective mass matrix.

2.3. Kinematic constraints

For insects and FWMAVs, there might exist kinematic constraints on the wing rigid-body rotations. For instance, the sweeping motion is generally controlled by a drive system, and a certain type of heaving motion or no heaving motion is generally enforced. If there are n_c rotational constraints, the number of independent generalized coordinates n_i will be $n + 4 - n_\text{c}$. The equations of motion given by Eq. 30 can be rewritten in a partitioned form as

$$\begin{bmatrix} \boldsymbol{M}_{n_\text{c}\times n_\text{c}} & \boldsymbol{M}_{n_\text{c}\times n_\text{i}} \\ \boldsymbol{M}_{n_\text{i}\times n_\text{c}} & \boldsymbol{M}_{n_\text{i}\times n_\text{i}} \end{bmatrix} \begin{bmatrix} \ddot{\boldsymbol{q}}_{n_\text{c}\times 1} \\ \ddot{\boldsymbol{q}}_{n_\text{i}\times 1} \end{bmatrix} = - \begin{bmatrix} \boldsymbol{0} \\ \boldsymbol{Q}^{\text{ela}}_{n_\text{i}\times 1} \end{bmatrix} + \begin{bmatrix} \boldsymbol{Q}^{\text{drive}}_{n_\text{c}\times 1} \\ \boldsymbol{0} \end{bmatrix} + \begin{bmatrix} \tilde{\boldsymbol{Q}}^{\text{aero}}_{n_\text{c}\times 1} \\ \tilde{\boldsymbol{Q}}^{\text{aero}}_{n_\text{i}\times 1} \end{bmatrix} - \begin{bmatrix} \boldsymbol{Q}^{\text{v}}_{n_\text{c}\times 1} \\ \boldsymbol{Q}^{\text{v}}_{n_\text{i}\times 1} \end{bmatrix}, \tag{31}$$

of which the unknown terms are $\ddot{\boldsymbol{q}}_{n_\text{i}\times 1}$ and $\boldsymbol{Q}^{\text{drive}}_{n_\text{c}\times 1}$. Therefore, two set of equations can be obtained, namely

$$\boldsymbol{Q}^{\text{drive}}_{n_\text{c}\times 1} = \boldsymbol{M}_{n_\text{c}\times n_\text{c}} \ddot{\boldsymbol{q}}_{n_\text{c}\times 1} + \boldsymbol{M}_{n_\text{c}\times n_\text{i}} \ddot{\boldsymbol{q}}_{n_\text{i}\times 1} - \tilde{\boldsymbol{Q}}^{\text{aero}}_{n_\text{c}\times 1} + \boldsymbol{Q}^{\text{v}}_{n_\text{c}\times 1}, \tag{32}$$

and

$$\boldsymbol{M}_{n_\text{i}\times n_\text{i}} \ddot{\boldsymbol{q}}_{n_\text{i}\times 1} = -\boldsymbol{Q}^{\text{ela}}_{n_\text{i}\times 1} + \tilde{\boldsymbol{Q}}^{\text{aero}}_{n_\text{i}\times 1} - \boldsymbol{Q}^{\text{v}}_{n_\text{i}\times 1} - \boldsymbol{M}_{n_\text{i}\times n_\text{c}} \ddot{\boldsymbol{q}}_{n_\text{c}\times 1}. \tag{33}$$

The latter equation represents the set of independent equations of motion. The last term in its right-hand side refers to the Euler force due to the prescribed rotational acceleration. By solving Eq. 33, the motion of a twistable wing can be obtained. Substituting Eq. 33 into Eq. 32, we get

$$\begin{aligned}\boldsymbol{Q}^{\text{drive}}_{n_c\times 1} = &\underbrace{\left[\boldsymbol{M}_{n_c\times n_c} - \boldsymbol{M}_{n_c\times n_i}\boldsymbol{M}^{-1}_{n_i\times n_i}\boldsymbol{M}_{n_i\times n_c}\right]\ddot{\boldsymbol{q}}_{n_c\times 1} - \boldsymbol{M}_{n_c\times n_i}\boldsymbol{M}^{-1}_{n_i\times n_i}\boldsymbol{Q}^{\text{v}}_{n_i\times 1} + \boldsymbol{Q}^{\text{v}}_{n_c\times 1}}_{\text{inertial terms}} \\ &\underbrace{+\boldsymbol{M}_{n_c\times n_i}\boldsymbol{M}^{-1}_{n_i\times n_i}\tilde{\boldsymbol{Q}}^{\text{aero}}_{n_i\times 1} - \tilde{\boldsymbol{Q}}^{\text{aero}}_{n_c\times 1}}_{\text{aerodynamic terms}} \underbrace{-\boldsymbol{M}_{n_c\times n_i}\boldsymbol{M}^{-1}_{n_i\times n_i}\boldsymbol{Q}^{\text{ela}}_{n_i\times 1}}_{\text{elastic terms}},\end{aligned} \tag{34}$$

from which it can seen that $\boldsymbol{Q}^{\text{drive}}_{n_c\times 1}$ is used to accelerate/decelerate the wing, overcome the aerodynamic drag and resist the elastic force, as represented by the inertial, aerodynamic and elastic terms, respectively. In practice, $\boldsymbol{Q}^{\text{drive}}_{n_c\times 1}$ is the drive torque which is applied by the motor of FW-MAVs or the thorax of insects. It can be used to determine the power consumption.

3. Validation of the proposed twist model

To validate the proposed twist model, we set the span, aspect ratio and the mass of the rectangular wing as 50 mm, 2.5 and 50 mg, respectively, by referring to the adult hawkmoth (HMF2) (Willmott and Ellington, 1997b) and artificial wings of similar size (Bolsman *et al.*, 2009). The wing thickness is set as 1 mm. Here the average thickness of the wing of HMF2 (about 35 μm) is not referred to for two reasons. First, the average thickness is not adequate to reflect the real hawkmoth wing thickness distribution considering its morphological complexity. Second, the wing with prescribed dimensions and mass can be easily fabricated using a foam sheet (Expanded PolyStyrene) (Peters *et al.*, 2017) in case artificial wings are needed for futural experimental study. A harmonic sweeping motion, $\phi(t) = \phi_m \sin(2\pi f t)$, is applied to drive the wing, where the amplitude ϕ_m is set to 60° and f is the flapping frequency. The heaving motion is restricted, i.e., $\theta(t) = 0$. The wing pitches passively due to the inertial and aerodynamic loads. The wing stiffness is modeled as a combination of the stiffness k_η of a torsional spring at the wing root and the distributed stiffness of the wing plate. The distributed stiffness is controlled by the Young's modulus E.

The first step before application of the proposed fluid-structure interaction (FSI) model is to determine the proper polynomial order in Eq. 4 such that the wing twist can be accurately represented. Therefore, the frequency f and the stiffness k_η are temporarily set to 25 Hz and 5×10^{-4} Nm/rad, which are close to the values of the referred wings. To study different wing stiffnesses, the Young's modulus is set to 1×10^8 Pa, 1×10^7 Pa, 1×10^6 Pa and 1×10^5 Pa. For each case, the convergence of the dynamic wing twist is checked by increasing the polynomial order from 1st- to 5th-order, as shown in Fig. 4. It can be observed for all the cases that (1) the twist based on the linear model deviates slightly from higher order twist models, and (2) the differences between the quadratic twist model and higher order twist models are negligible. The marginal contribution of twist modes that are higher than 2nd-order can be explained by the fact that the inertial and aerodynamic loads increase roughly linearly and quadratically from the wing root to the tip, respectively. Therefore, the quadratic polynomial is used for studying the rectangular wing twist. The corresponding degrees of freedom are the twist angles of the chords at the half-span and the tip, i.e., q_1^{ela} and q_2^{ela}. Combining this quadratic twist description and the wing tip displacement $u^{\text{tip}}_{x_c}$, the elastic displacement of the entire wing can be analytically described by Eq. 3.

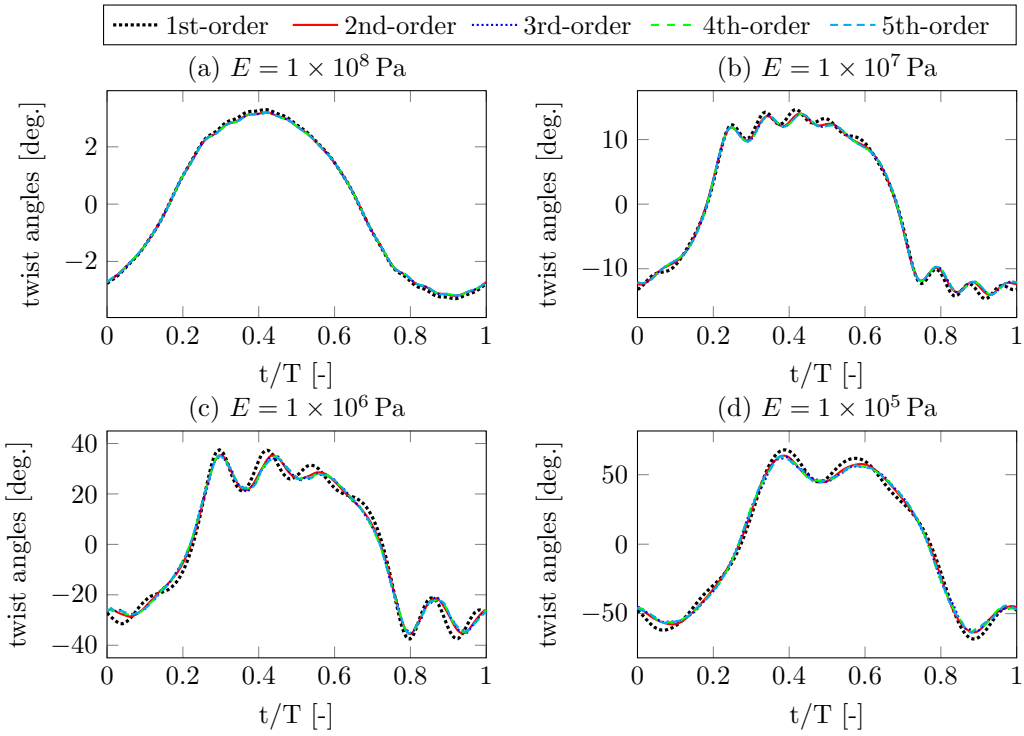

Figure 4: Comparison of the wing dynamic twist when different orders of polynomials (from the 1st- to the 5th-order) are used to describe the twist angle along the span. Wings with different Young's moduli are investigated from (a) to (d).

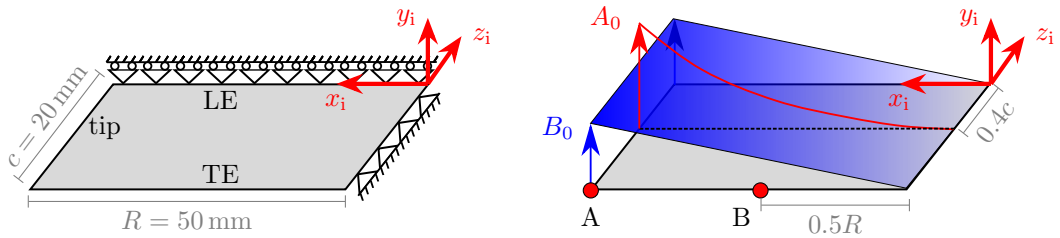

(a) boundary conditions (b) loading conditions

Figure 5: Boundary conditions and loading cases of the rectangular plate used for validating the proposed plate model. (a) The boundary conditions are applied on the leading edge (LE) and the root chord of the middle surface. (b) Two loading cases are considered. The aerodynamic load, which is applied at the 40% chord line, increases quadratically from zero at the root to A_0 at the tip. The inertial load distributes uniformly along the chord direction and linearly increases from zero at the root to B_0 at the tip. The points A and B are located at the tip and middle of the trailing edge (TE), respectively.

In addition to the analytical description of the wing elastic displacement, the proposed twist model uses the nonlinear strain-displacement relations as given by Eq. 20. To validate the proposed twist model, especially for large twist, we calculate and compare the twist using both the proposed model and a finite element analysis (FEA) using COMSOL Multiphysics® software. In FEA, quadratic hexahedral elements ($2 \times 40 \times 100$) are used. The mesh size was selected

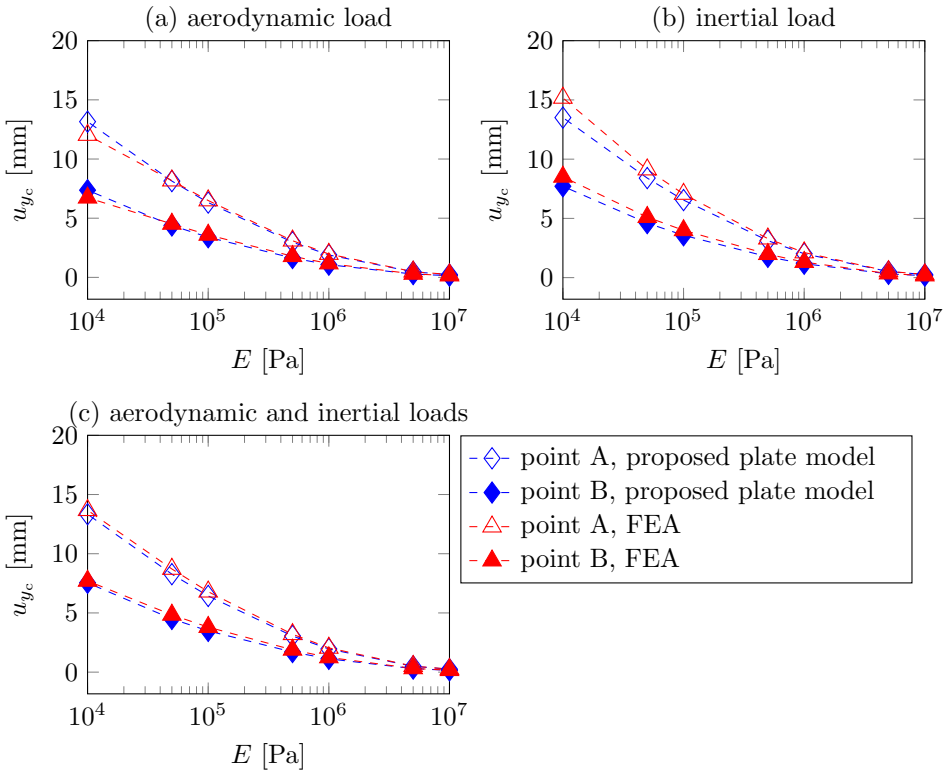

Figure 6: Comparison of the out-of-plane displacements u_{y_c} of statically loaded plates based on the proposed analytical plate model and the FEA using COMSOL Multiphysics® software. Three loading cases are considered. (a) The aerodynamic load with $A_0 = 6 \times 10^{-2}$ N/m is applied. (b) The inertial load with $B_0 = 2\,\text{N/m}^2$ is applied. (c) Both the aerodynamic and inertial loads are applied. The values of A_0 and B_0 are equal to 3×10^{-2} N/m and $1\,\text{N/m}^2$, respectively. The values of A_0 and B_0 guarantee the same resultant force for all the three cases.

based on convergence analysis. For both the FEA and the proposed model, linear elasticity is assumed, and Newton method is used to solve the nonlinear equations. Based on the analytical displacement description in Eq. 3, the boundary conditions for the FEA can be obtained, as illustrated in Fig. 5 (a). All the boundary conditions are applied at the edges of the wing's middle surface. Two types of loads are considered as shown in Fig. 5 (b). The aerodynamic load, which is applied at the 40% chord line, increases quadratically from zero at the root to A_0 at the tip. The 40% chord line is chosen to roughly represent the chordwise aerodynamic load center which might vary from the 1/4 chord to the 1/2 chord in reality (Han *et al.*, 2015). The inertial load distributes uniformly along the chord direction and linearly increases from zero at the root to B_0 at the tip. This load results from the acceleration of the sweeping motion, which can be dominant as compared to other inertial terms (Ennos, 1989). Using these loads, three static loading cases are studied for the validation. Case (a) considers the aerodynamic load with $A_0 = 6 \times 10^{-2}$ N/m, while Case (b) includes the inertial load with $B_0 = 2\,\text{N/m}^2$. Case (c) considers both the aerodynamic and inertial loads with A_0 and B_0 being equal to 3×10^{-2} N/m and $1\,\text{N/m}^2$, respectively. The values of A_0 and B_0 guarantee the same resultant force for all the three cases.

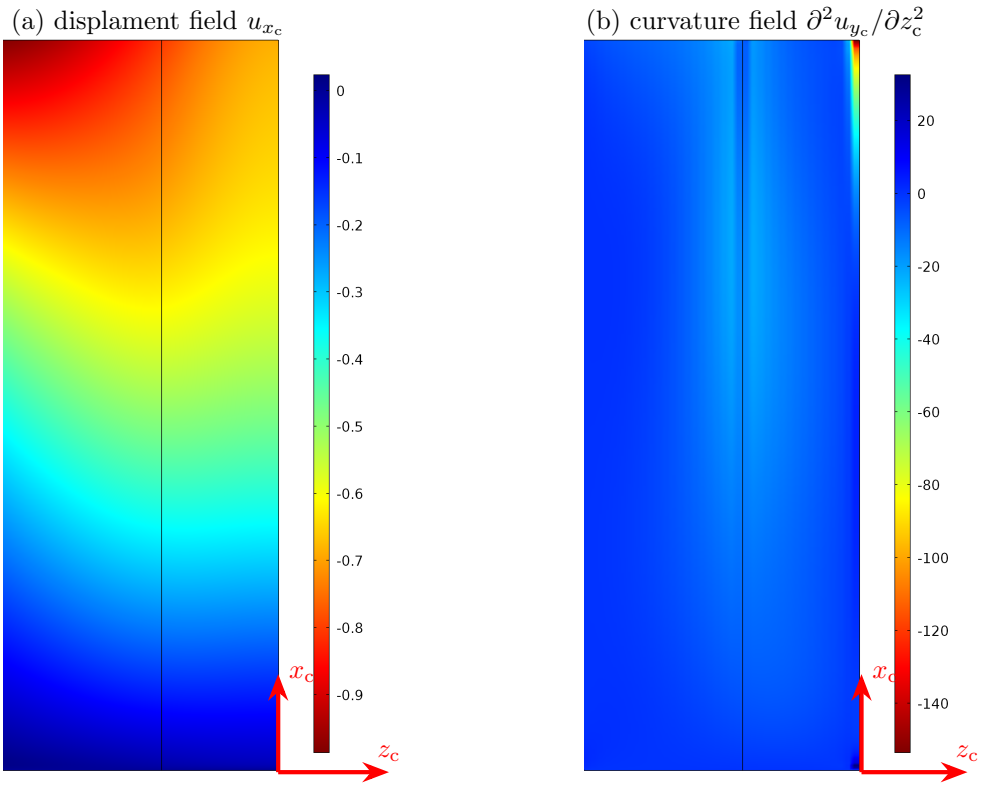

Figure 7: Numerical results plotted on the middle surface of the rectangular wing obtained by the FEA using COMSOL Multiphysics® software. The Young's modulus of the wing is 1×10^4 Pa, and the loading case (c) is applied. (a) spanwise displacement field u_{x_c} [mm]. (b) curvature field $\partial^2 u_{y_c}/\partial z_c^2$ [1/mm] which reflects the local chordwise camber. The black line indicates the location where the aerodynamic loads are applied.

For the three loading cases, the out-of-plane displacements u_{y_c} at the tip and middle of the TE (i.e., the points A and B in Fig. 5 (b)) are compared for the values obtained by the proposed model and the FEA. It can be seen from Fig. 6 that, for Case (a), the maximum errors at point A and B are about 15% and 11%, respectively, while for Case (b) they are around 11% at both locations. The errors for these two cases provide the extreme scenarios of the validity of the proposed plate model. Case (c) considers both the inertial and aerodynamic loads, and the maximum errors are only about 5% and 10% at point A and B, respectively. It is worth mentioning that the maximum twist angles for three loading cases are quite large (between 40° and 50°). The good accuracy of the proposed plate model for large twists can be attributed to the consideration of the wing shorting effect and the inclusion of the quadratic membrane terms in the strain-displacement relations. The errors are mainly induced by two assumptions used in the proposed twist model. First, the spanwise displacement is enforced to change linearly from the root to the tip. Second, the chordwise stretching and camber are ignored. In contrast, the FEA shows a more complicated spanwise displacement field due to the varying spanwise shortening from the LE to the TE, as shown by an example in Fig. 7 (a). Meanwhile, significant camber can be observed when the wing is subject to the prescribed aerodynamic loads (see Fig. 7 (b)).

4. Twist optimization

The proposed twist model and the quasi-steady aerodynamic model dramatically reduce the computational cost for the FSI analysis as compared to traditional FSI models. In our FSI simulations, the wing is discretized into 50 chordwise strips, which are adequate for the description of the quadratic wing twist. The wing's passive pitching motion normally starts to converge to its steady state from the second half of the first cycle. The aerodynamic force and power consumption in the third cycle are used for analysis and optimization. Newmark method with $\gamma = 1/2$ and $\beta = 1/4$ is used to solve the equations of motion while 500 time steps are taken for each cycle. Each simulation takes about only 4 minutes when using MATLAB® R2014b on a 64-bit computer with a RAM capacity of 8 GB and an Intel® Core™ i5 CPU at 3.40 GHz.

4.1. Optimization model

The proposed FSI model will be used to optimize the wing twist and kinematics which minimize the cycle-averaged power consumption during hovering flight. The design variables include the root stiffness k_η, the Young's modulus E and the flapping frequency f. The power can be calculated by

$$P^{\text{total}} = \dot{\boldsymbol{q}}^{\text{T}}_{n_c\times 1}\boldsymbol{Q}^{\text{drive}}_{n_c\times 1}, \tag{35}$$

where $\boldsymbol{Q}^{\text{drive}}_{n_c\times 1}$ and $\dot{\boldsymbol{q}}_{n_c\times 1}$ are the drive torque and generalized velocity, respectively. Similar to Eq. 34, the total power can be decomposed into three components, namely the aerodynamic power P^{aero}, inertial power P^{iner} and the elastic power P^{ela}. Note, the power can be negative due to the loss of the kinetic energy during the deceleration. The lost kinetic energy can be dissipated, used to compensate the energy consumed by the aerodynamic drag, or stored in a kinetic energy recovery drive system (KERS). KERS can appear in different forms, e.g., insect thoraxes (Dudley, 2002) and elastic structures of FWMAVs (Bolsman *et al.*, 2009; Lau *et al.*, 2014). The uncertainty in the kinetic energy transformation complicates the modeling of the average power consumption. Instead, two extreme power consumption scenarios are modeled. First, an ideal KERS is used, which implies that the average elastic and inertia power are both zero. In this setting, the total average power is equal to the average aerodynamic power, i.e.,

$$\bar{P}^{\text{total}}_{\text{KERS}} = \frac{1}{T}\int_T P^{\text{total}}dt = \frac{1}{T}\int_T P^{\text{aero}}dt, \tag{36}$$

with T representing the period of a flapping cycle. Second, a drive system which can not recover any energy is adopted. In this case, the kinetic and elastic energy first compensate the energy consumed by drag. Then, extra energy will be dissipated. This type of drive system will be referred to as non-KERS. The total average power for this extreme case can be calculated by

$$\bar{P}^{\text{total}}_{\text{non-KERS}} = \frac{1}{T}\int_T \Xi\left(P^{\text{total}}\right)dt, \tag{37}$$

where $\Xi(\bullet)$ is an operator which sets negative values to zero but keeps positive values. In practice, the power consumed by flapping wings lies between $\bar{P}^{\text{total}}_{\text{KERS}}$ and $\bar{P}^{\text{total}}_{\text{non-KERS}}$.

For convenience, the optimization with three design variables (i.e., f, k_η and E) is denoted as the "full optimization". In addition, two other optimization cases are studied. One case prescribes the flapping frequency and optimizes the values of k_η and E, while the second case prescribes the root stiffness and optimizes the values of f and E. For all cases, the same objective function and lift constraint are used. By referring to wings of similar size (Willmott and Ellington, 1997b; Bolsman *et al.*, 2009), the required average lift is set to 1 g per wing. The optimized twistable wings will be compared with the corresponding optimized rigid wings for all the cases.

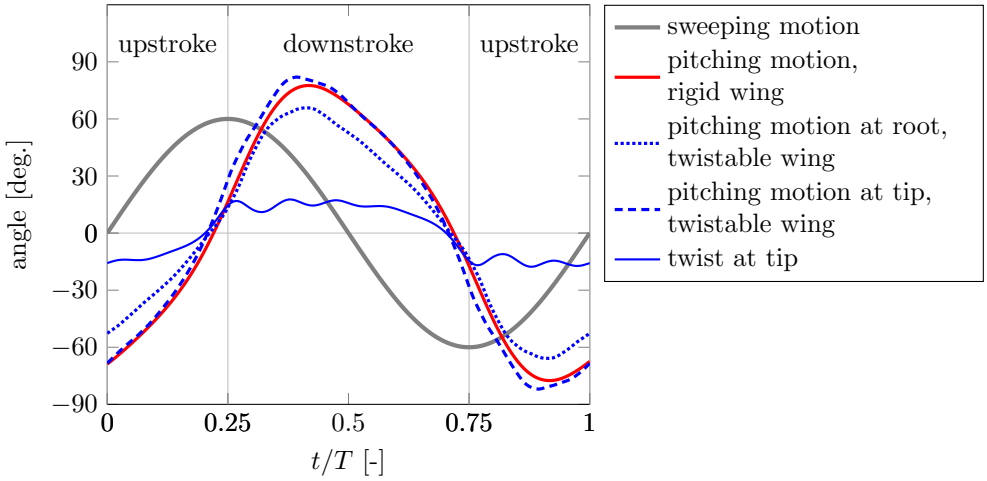

Figure 8: Comparison of the pitching motion for the optimized twistable and rigid wings.

4.2. Optimization results and analysis

In the following three subsections, the optimal wing designs for KERS are studied. At the end of this section, the optimal designs for KERS and non-KERS will be compared.

4.2.1. Case 1: full optimization

Previous studies (Du and Sun, 2008, 2010; Nakata and Liu, 2012a,b; Dai *et al.*, 2012) show that twistable flapping wings can outperform their rigid counterparts in terms of power efficiency during hovering flight. However, the kinematics of the rigid counterparts was generally not optimized. In contrast, we optimize the flapping frequency and wing stiffness for both twistable and rigid wings and compare the resulting power efficiency. The design parameters for twistable wings are f, k_η and E, while f and k_η are optimized for rigid wings.

Optimization shows that the cycle-averaged power consumption for optimized twistable and rigid wings are 39.77 W/kg and 40.57 W/kg, respectively. The power has been normalized by the lift generation per kilogram. The improvement in power efficiency by incorporating twist is about 2 percents. In contrast, more considerable improvements were reported in previous studies which normally provide comparisons of unoptimized twistable and rigid wings. For KERS, the total power is equal to the aerodynamic power which is proportional to the drag and the flapping velocity. Therefore, in order to explain the marginal difference in power efficiency, both the optimal pitching motion and the corresponding aerodynamic forces are compared for the optimized twistable and rigid wings.

The pitching motion of the optimized wings is compared in Fig. 8. It can be observed that the optimized rigid wing pitches at a high amplitude (77.56°). Considering that the resultant aerodynamic force is regarded to be perpendicular to the chord throughout a flapping cycle, the higher pitching amplitude leads to a higher cycle-averaged lift-to-drag ratio. Since the average lift has been fixed, a higher lift-to-drag ratio implies a lower average drag. For the twistable wing, the optimal design has a root stiffness of 2.88×10^{-4} Nm/rad and Young's modulus of 3.67×10^6 Pa. The root stiffness is slightly larger than the optimal stiffness of the rigid wing (2.39×10^{-4} Nm/rad), which leads to a slightly lower pitching amplitude at the root of the twistable wing

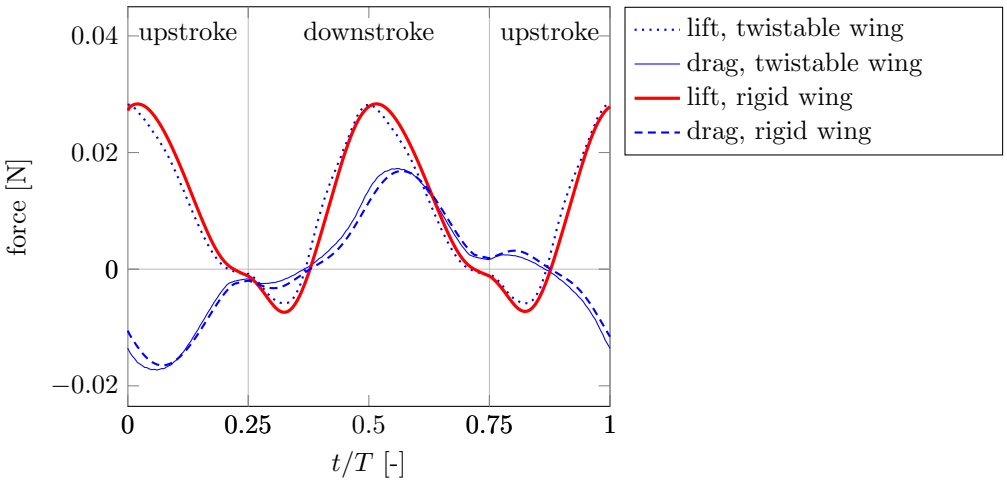

Figure 9: Comparison of the lift and drag generated by the optimized twistable and rigid wings.

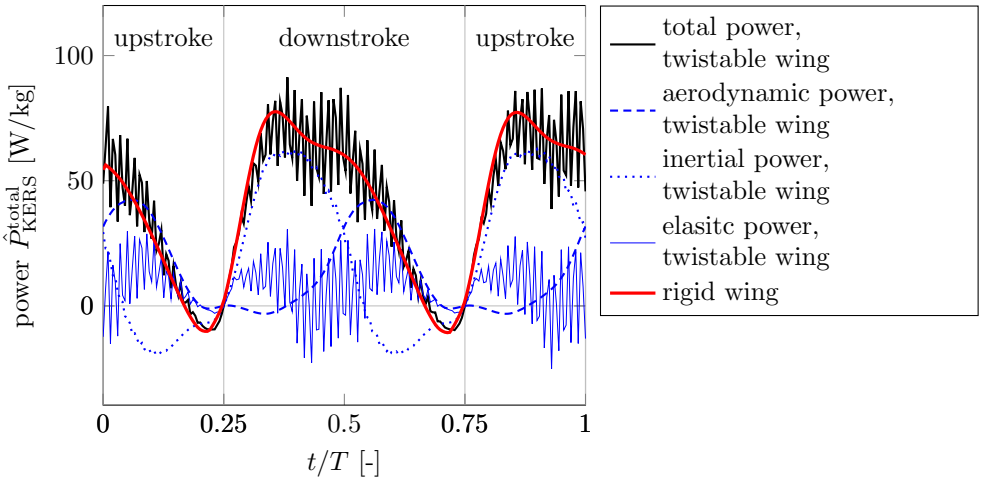

Figure 10: Comparison of the power history of the optimized twistable and rigid wings.

as shown in Fig. 8. However, with the help of the wing flexibility, a twist with an amplitude of 17.68° exhibits for the optimized twistable wing. Due to the twist, the pitching amplitude at the tip is higher than the optimized rigid wing. Nevertheless, Figure 9 shows that the wing twist does not dramatically change the lift and drag profiles. Furthermore, the optimum frequency for the twistable wing and the rigid wing are 20.24 Hz and 20.63 Hz, respectively. The comparable drag profiles and flapping frequencies of the optimized twistable and rigid wings explain the marginal difference in power efficiency.

The power history for the optimized twistable and rigid wings is compared in Fig. 10. The most obvious difference is that the power for the rigid wing is very smooth while there exist high frequency oscillations for the twistable wing. From the decomposition of the total power for the

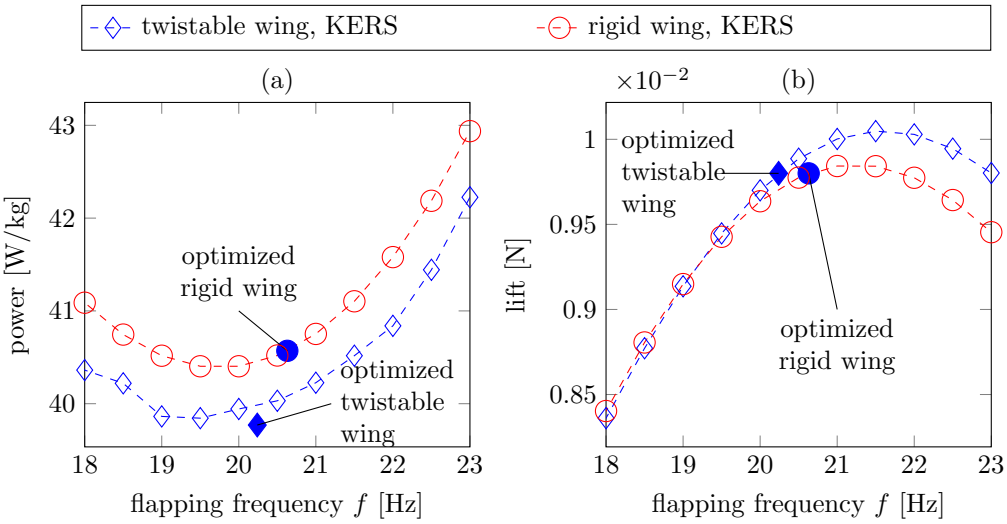

Figure 11: Sensitivity of the power consumption and lift generation of twistable and rigid wings with respect to the flapping frequency when the other parameters are fixed at their optimal values. A KERS drive system is used.

twistable wing, we can see that the high frequency component originates from the elastic power. The elastic power is partially used to deform the wing in spanwise direction. Due to the high axial stiffness, the highest undamped eigenfrequency of the optimized twistable wing is about 80 times the optimum flapping frequency. Moreover, this high frequency spanwise motion is hardly damped since the aerodynamic load acts perpendicular to the spanwise axis. Therefore, it is not surprising to see the high frequency components of the elastic power and, thus, the total power.

When an optimized twistable or rigid wing is adopted, the flapping frequency might deviate from the optimum for maneuvering. Thus, Fig. 11 shows the sensitivity of the power consumption and lift generation of twistable and rigid wings with respect to the frequency when all the other parameters are fixed at their optimal values. It can be observed that the effects of the frequency on the power efficiency are comparable between twistable and rigid wings for a KERS drive system. However, the lift generation can be increased by driving the optimized twistable wing with a higher frequency, while there is hardly any potential for the optimized rigid wing to increase lift generation by changing the frequency. The difference underlines the advantage of the twistable wing in terms of flight control.

4.2.2. Case 2: optimization of wings with prescribed frequencies

The drive frequency of a FWMAV can significantly deviate from the optimum frequency due to hardware limitations, control operations and payload change. Therefore, it is useful to study the influence of wing twist on power efficiency when the flapping frequency is prescribed differently from the optimum drive frequency (i.e., 20.24 Hz). In this subsection, we optimize k_η for the rigid wings and both k_η and E for twistable wings. The wings will be driven at different frequencies that range from 20 Hz to 30 Hz with a step size of 1 Hz.

The power efficiency and optimal designs are compared in Fig. 12. It can be seen from Fig. 12 (a) that when the drive frequency is fixed at different non-optimal values, the power saved by the optimized twistable wings is very limited when compared to corresponding rigid wings.

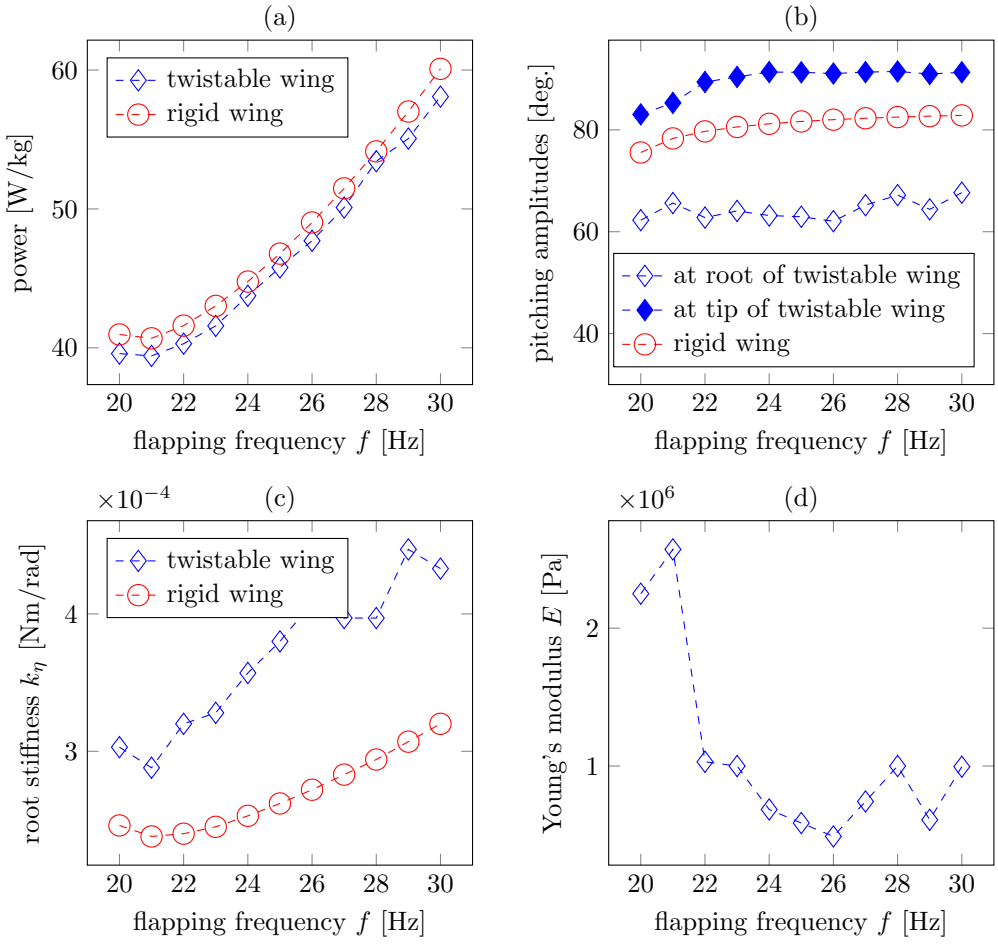

Figure 12: Comparison of optimized twistable and rigid wings when the drive frequency is fixed at different values.

Meanwhile, the drive frequency can dramatically change the power consumption of optimized wings. Figure 12 (b) shows that the pitching amplitudes of the optimized rigid wings are between the pitching amplitudes at the root and the tip of the corresponding optimized twistable wings. The difference of the pitching motion of the optimized twistable and rigid wings for different drive frequencies are quite similar to what we have shown in Fig. 8.

Figures 12 (c) and (d) show the wing root stiffness and the Young's modulus of the optimized wings. We can see from Fig. 12 (c) that the root stiffness of optimized twistable wings is always higher than for corresponding rigid wings, which results in lower pitching amplitudes at the root of the twistable wings. In addition, the optimal root stiffness (Fig. 12 (c)) for the rigid wings changes smoothly with the frequency. However, both the wing root stiffness (Fig. 12 (c)) and Young's modulus (Fig. 12 (d)) for the twistable wings are non-smooth. In contrast, the resulting power consumption for the optimized twistable wings is quite smooth. To explain this, we plot the contour lines of the lift and power as a function of the root stiffness and Young's modulus.

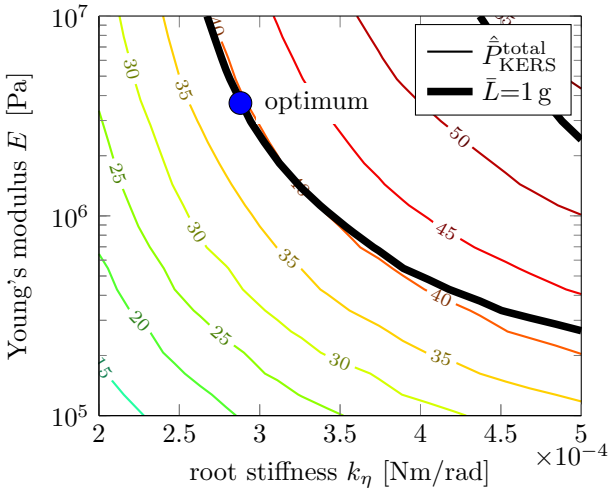

Figure 13: Contour plots of the lift and the power consumption as a function of the root stiffness and Young's modulus. The lift acts as a constraint in the optimization. The lift constraint is included as a thick solid line. The blue dot represents the wing stiffness of the optimized twistable wing based on the full optimization.

It can be observed that, near the optimal design, the lift contour line with a value equal to the required lift generation is approximately parallel to the contour lines for power consumption. This indicates that twistable wings with different combinations of root stiffness and Young's modulus can have similar power efficiency. This phenomenon can be explained by the fact that both the change of root stiffness and the Young's modulus can alter the overall pitching motion and, thus, the aerodynamic power. Furthermore, the freedom on choosing the root stiffness and Young's modulus provides more space for the power-efficient wing designs.

4.2.3. Case 3: optimization of wings with fixed root stiffness

In nature, some insects use pitching motion with high amplitudes but small twist, while others show very small pitching amplitudes at the wing root but large twist. These observations imply that the usefulness of wing twist might be related to the pitching motion at the root. Therefore, we investigate the power efficiency of optimized twistable wings when different values of the root stiffness are used. In this subsection, we optimize f for the rigid wings and both f and E for twistable wings when the root stiffness varies from 3×10^{-4} Nm/rad to 1×10^{-3} Nm/rad with a step size of 1×10^{-4} Nm/rad.

The comparison of the optimized twistable and rigid wings is shown in Fig. 14. From Fig. 14 (a) and (b), it can be observed that both the power consumption and the flapping frequency for optimized rigid wings approximately increase linearly with the root stiffness. In contrast, both the power consumption and the frequency only show a slight increase for optimized twistable wings. Figure. 14 (c) shows that the pitching amplitude of the optimized rigid wings decreases with the root stiffness, while the twist angle of the optimized twistable wing increases. To increase the twist angle for twistable wings, the Young's modulus needs to decrease, as demonstrated in Fig. 14 (d).

The different responses of the power consumption with the increase of the root stiffness can be explained by combining the optimal flapping frequency and the pitching amplitudes as shown

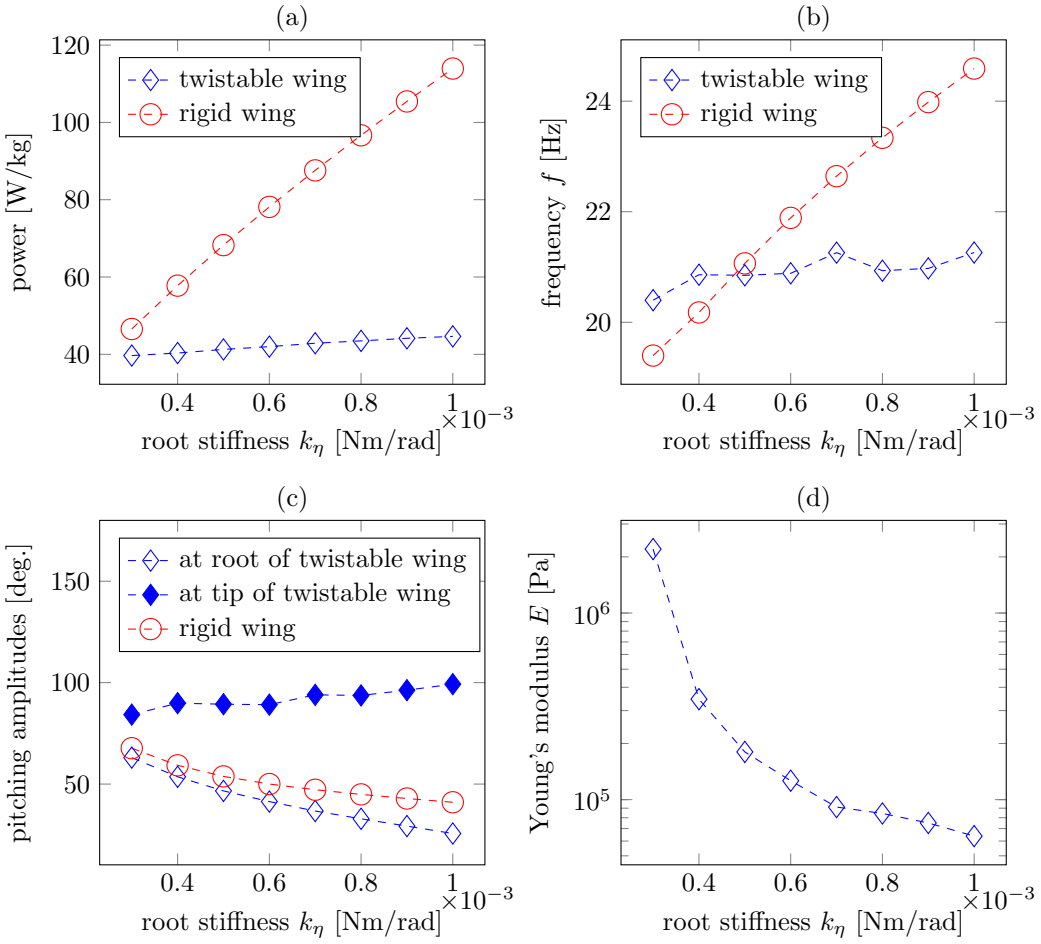

Figure 14: Comparison of the optimized twistable and rigid wings when the root stiffness is fixed at different values.

in Fig. 14 (b) and (c), respectively. As explained in Sec. 4.2.1, the decreasing pitching amplitude tends to increase the average drag, and the increase of the drive frequency tends to increase the flapping velocity. Increase of the average drag and the flapping velocity both lead to higher power consumption for optimized rigid wings. For optimized twistable wings, the increases of the twist and the drive frequency have an opposite effect to the power efficiency. Therefore, the power consumption of optimized twistable wings does not change dramatically for different root stiffness.

The optimization results can be also interpreted from the perspective of lift generation. For rigid wings, due to the decrease of the pitching amplitude, the lift coefficient tends to get lower. In order to maintain sufficient lift generation, the flapping frequency needs to increase. In contrast, wing twist helps to maintain the overall angle of attack when the pitching amplitudes at the root gets lower due to an increase of the root stiffness. As a result, the optimal frequency of the optimized twistable wing does not change as much as for rigid wings.

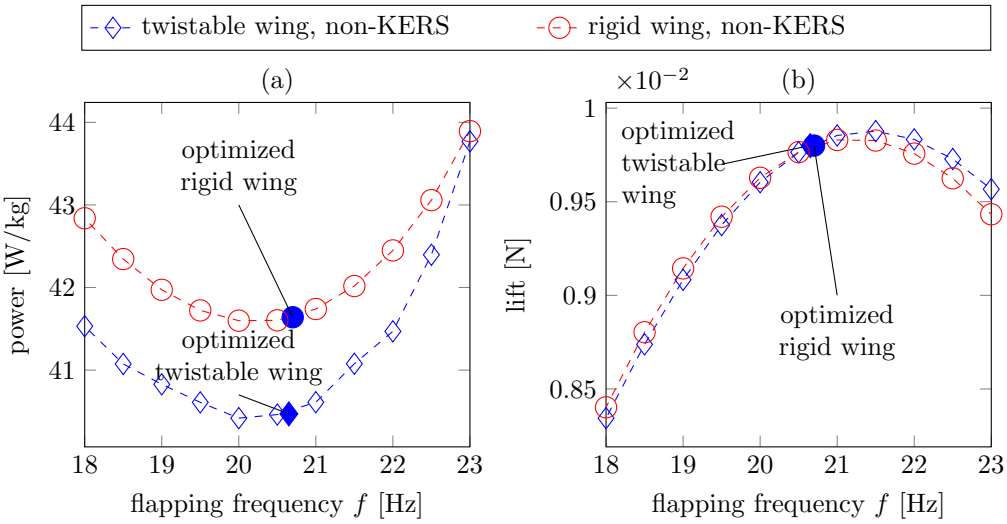

Figure 15: Sensitivity of the power consumption and lift generation of twistable and rigid wings with respect to the flapping frequency when the other parameters are fixed at their optimal values. A non-KERS drive system is used.

4.2.4. Comparison between KERS and non-KERS

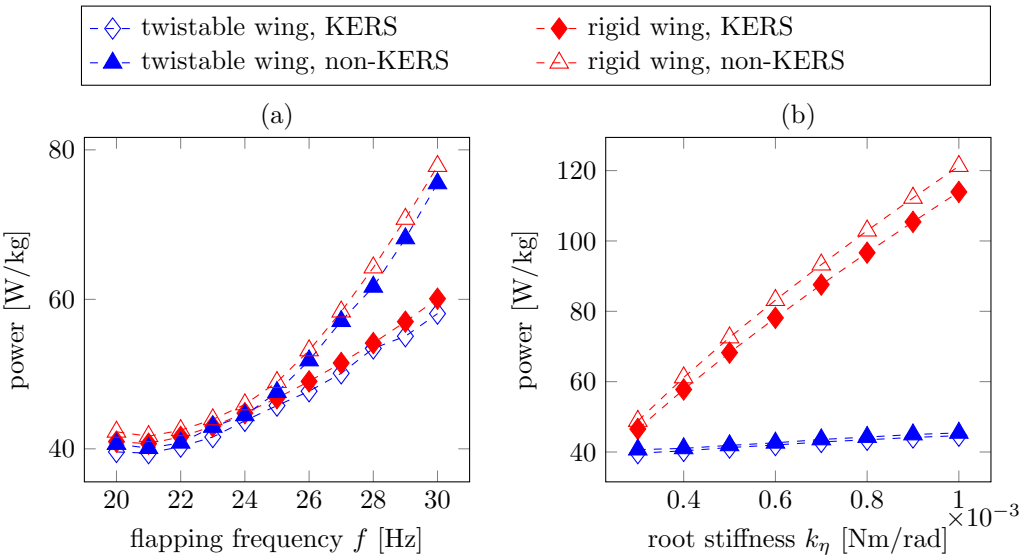

Figure 16: Comparison of power efficiency of optimized wing designs for KERS and non-KERS drive systems. (a) The flapping frequency is fixed at different values. (b) The root stiffness is prescribed.

The studies in the previous subsections assumed a KERS drive system. For a non-KERS drive system, the optimal frequencies for fully optimized twistable and rigid wings, similar to the study in Case 1, are 20.65 Hz and 20.70 Hz, respectively. The corresponding power consumptions are

40.47 W/kg and 41.64 W/kg. The improvement in power efficiency by incorporating twist is about only 3 percents, which is close to the value for KERS (about 2 percents). Figure 15 shows the sensitivity analysis of the power consumption and lift generation with respect to the flapping frequency when the other parameters are fixed at their optimal values. It can be observed that the power efficiency of twistable wings is getting closer to the rigid wings when the frequency increases from the optimal values. The corresponding increase of lift for twistable wings is marginal, which is different from the effect for the KERS system.

In Fig. 16, we compare the power efficiency of optimized wings for KERS and non-KERS when the drive frequency or the root stiffness is prescribed, similar to Cases 2 and 3 as studied in the previous subsections. From Fig. 16 (a), it can be observed that KERS and non-KERS show very similar power efficiency when the frequency is close to the optimum (i.e., 20.24 Hz). However, when the drive frequency significantly deviates from the optimum, the difference of the power consumption becomes more considerable. For instance, when the frequency is fixed at 30 Hz, the optimized twistable wing can save about 23% of the power for KERS as compared to non-KERS. Figure 16 (b) shows that, for the optimized twistable wings, the power efficiency does not change significantly with the prescribed root stiffness when a non-KERS system is used. This is similar to the observation for KERS. Meanwhile, the difference between the power consumed for KERS and non-KERS are negligible for all the root stiffness. For optimized rigid wings, the difference between the power consumed by KERS and non-KERS slightly increases with the root stiffness but is still not very pronounced.

5. Conclusions and outlook

We have proposed a computationally efficient Fluid-Structure Interaction (FSI) model to enable the parametric study and optimization of flapping wing twist and corresponding kinematics. The proposed FSI model relies on an analytical twist model and a quasi-steady aerodynamic model. The twist model uses a polynomial to describe the change of the twist angle along the span. The spanwise shortening effect and the quadratic strain-displacement relations for the wing membrane deformation have been included to guarantee accuracy for large twist. It has been shown for rectangular wings that a quadratic polynomial can accurately model the twist at large amplitudes. Moreover, the proposed twist model and the quasi-steady aerodynamic model enable full FSI analysis in just a few minutes, which demonstrates the computational efficiency of the proposed FSI model.

Based on the proposed FSI model, we have optimized the stiffness and flapping frequency for both rigid and twistable wings to minimize the power consumption for hovering. Comparisons show that the optimized twistable wings exhibit power efficiency close to the optimized rigid wings, unless the pitching amplitude at the wing root is limited. This conclusion can be explained by the fact that the power efficiency is influenced by the overall angle of attack which determines the lift-to-drag ratio. This optimal value can be achieved by both the pitching of the entire rigid wing and the spanwise twist of the twistable wing. When the pitching amplitude at the root decreases by increasing the root stiffness, the optimized rigid wings need more power for hovering. However, the power efficiencies of optimized twistable wings with different prescribed root stiffness are comparable with the twistable wings with optimal root stiffness. This observation provides an explanation for the different levels of twist demonstrated by insect wings.

Although only rectangular wings have been used in this study to separate wing twist from wing shape, the proposed FSI model can be applied to wings with more complex shapes and

kinematics. Therefore, the computational efficiency of the proposed FSI model allows parametric study and optimization of flapping wings to enhance the understanding of insect wing flexibility and may help the design of flexible artificial wings for FWMAVs. For wings with an inhomogeneous and anisotropic structure, the wing camber might be more prominent in additional to more complex twist behavior. For such cases, the structural analysis of the FSI model can be updated by using higher order analytical models or finite element models, and an update on the quasi-steady aerodynamic model by including the contribution from the wing camber might be required.

Acknowledgements

This work is financially supported by China Scholarship Council (CSC NO. 201206290060).

Appendix A. Quasi-steady aerodynamic model

The aerodynamic force is calculated by the predictive quasi-steady aerodynamic model proposed by Wang *et al.* (2016). The quasi-steady model calculates the resultant force $dF^{\text{aero}}_{y_\text{e}}$ on a strip with an infinitesimal width dx_e by including four loading terms, i.e.,

$$dF^{\text{aero}}_{y_\text{e}} = \left(\tilde{F}^{\text{trans}}_{y_\text{e}} + \tilde{F}^{\text{rot}}_{y_\text{e}} + \tilde{F}^{\text{coupl}}_{y_\text{e}} + \tilde{F}^{\text{am}}_{y_\text{e}}\right) dx_\text{e}, \tag{A.1}$$

where $\tilde{F}^{\text{trans}}_{y_\text{e}}$, $\tilde{F}^{\text{rot}}_{y_\text{e}}$, $\tilde{F}^{\text{coupl}}_{y_\text{e}}$ and $\tilde{F}^{\text{am}}_{y_\text{e}}$ represent the force components resulting from the translation, the rotation, their coupling and the added-mass effect of the strip with unit width, respectively.

The translation-induced force is formulated as

$$\tilde{F}^{\text{trans}}_{y_\text{e}} = -\text{sgn}\left(v_{y_\text{e}}\right) \frac{1}{2}\rho^\text{f} \tilde{v}^2 C^{\text{trans}} c, \tag{A.2}$$

of which $\text{sgn}(\cdot)$ is the signum function, v_{y_e} is the component of the velocity $\boldsymbol{v}_\text{e}$ on the y_e axis, ρ^f is the fluid density and C^{trans} is the translational force coefficient. C^{trans} is calculated by

$$C^{\text{trans}} = 2\pi \mathit{AR} \sin\left(\tilde{\alpha}\right) \left(2 + \sqrt{\mathit{AR}^2 + 4}\right)^{-1}, \tag{A.3}$$

with AR representing the wing aspect ratio defined as R/c, and $\tilde{\alpha}$ the angle of attack. The corresponding location of center of pressure (CP) $\hat{d}^{\text{trans}}_{\text{cp}} = |\tilde{\alpha}|/\pi$. The CP location is defined as the local-chord-length normalized distance between the pitching axis and the CP, which also holds for the CP of the other three loading terms.

The rotation-induced force is calculated by

$$\tilde{F}^{\text{rot}}_{y_\text{e}} = \left[\text{sgn}(\omega_{x_\text{e}}) \int_{\hat{d}c-c}^{\hat{d}c} \text{sgn}(z_\text{e}) \frac{1}{2}\rho^\text{f} \omega^2_{x_\text{e}} z^2_\text{e} C^{\text{rot}} dz_\text{e}\right], \tag{A.4}$$

where C^{rot} is the rotational damping coefficient, which takes the value of the translational force coefficient C^{trans} when the angle of attack $\tilde{\alpha}$ is $\pi/2$. The corresponding CP $\hat{d}^{\text{rot}}_{\text{cp}} = 3/4$.

The force due to the coupling between the strip translation and rotation is formulated as

$$\tilde{F}^{\text{coupl}}_{y_\text{e}} = \tilde{F}^{\text{coupl,I}}_{y_\text{e}} + \tilde{F}^{\text{coupl,II}}_{y_\text{e}} = \begin{cases} \left(\hat{d} - \frac{3}{4}\right)\pi\rho^\text{f} c^2 \omega_{x_\text{e}} v_{z_\text{e}} - \frac{1}{4}\pi\rho^\text{f} c^2 \omega_{x_\text{e}} v_{z_\text{e}} & \text{if } \tilde{\alpha} \leqslant \pi/2 \\ \left(\frac{1}{4} - \hat{d}\right)\pi\rho^\text{f} c^2 \omega_{x_\text{e}} v_{z_\text{e}} - \frac{1}{4}\pi\rho^\text{f} c^2 \omega_{x_\text{e}} v_{z_\text{e}} & \text{if } \tilde{\alpha} > \pi/2 \end{cases}, \tag{A.5}$$

where $\tilde{F}_{\mathrm{c}}^{\mathrm{coupl,I}}$ results from the downwash flow at three-quarter chord induced by the wing rotation, and $\tilde{F}_{\mathrm{c}}^{\mathrm{coupl,II}}$ is a result of Coriolis effect experienced by the flow on a rotating wing. The component $\tilde{F}_{\mathrm{c}}^{\mathrm{coupl,I}}$ is formulated differently depending on the value of the angle of attack. When $\alpha \leqslant \pi/2$, the sweeping reversal is generally advanced to the pitching reversal. When $\tilde{\alpha} > \pi/2$, the sweeping reversal follows the pitching reversal. In this case, the incoming flow can be regarded to come from the trailing edge to leadin/g edge, which is opposite to the first case. Furthermore, these two force components act at different locations of the chord. The CP locations $\hat{d}_{\mathrm{cp}}^{\mathrm{coupl,I}}$ and $\hat{d}_{\mathrm{cp}}^{\mathrm{coupl,II}}$ are given by

$$\hat{d}_{\mathrm{cp}}^{\mathrm{coupl,I}} = \begin{cases} 1/4 & \text{if } \tilde{\alpha} \leqslant \pi/2 \\ 3/4 & \text{if } \tilde{\alpha} > \pi/2 \end{cases}, \quad \hat{d}_{\mathrm{cp}}^{\mathrm{coupl,II}} = \begin{cases} 3/4 & \text{if } \tilde{\alpha} \leqslant \pi/2 \\ 1/4 & \text{if } \tilde{\alpha} > \pi/2 \end{cases}. \tag{A.6}$$

The force due to the added-mass effect is calculated by

$$\tilde{F}_{y_{\mathrm{e}}}^{\mathrm{am}} = \tilde{F}_{y_{\mathrm{e}}}^{\mathrm{am,I}} + \tilde{F}_{y_{\mathrm{e}}}^{\mathrm{am,II}} = -\frac{\pi}{4}\rho^{\mathrm{f}} c^2 a_{y_{\mathrm{e}}} - \frac{\pi}{8}\left(1 - 2\hat{d}\right)\rho^{\mathrm{f}} c^3 \alpha_{x_{\mathrm{e}}}, \tag{A.7}$$

where $\tilde{F}_{y_{\mathrm{e}}}^{\mathrm{am,I}}$ and $\tilde{F}_{y_{\mathrm{e}}}^{\mathrm{am,II}}$ represent the inertial forces experienced by the wing strip when accelerating a virtual mass $\frac{\pi}{4}\rho^{\mathrm{f}} c^2$ and a virtual moment of inertia $\frac{\pi}{8}\rho^{\mathrm{f}} c^3$, respectively. The corresponding CP locations $\hat{d}_{\mathrm{cp}}^{\mathrm{am,I}} = 1/2$ and $\hat{d}_{\mathrm{cp}}^{\mathrm{am,II}} = 9/16$.

The resultant lift L and drag D are defined in the z_{i} and y_{i} axes of the inertial frame, respectively. They can be calculated by

$$L = \int_0^R \boldsymbol{e}_{z_{\mathrm{i}}}^{\mathrm{T}} \boldsymbol{R}_{\mathrm{e}\to\mathrm{i}} \boldsymbol{e}_{y_{\mathrm{e}}} dF_{y_{\mathrm{e}}}^{\mathrm{aero}} \quad \text{and} \quad D = \int_0^R \boldsymbol{e}_{y_{\mathrm{i}}}^{\mathrm{T}} \boldsymbol{R}_{\mathrm{e}\to\mathrm{i}} \boldsymbol{e}_{y_{\mathrm{e}}} dF_{y_{\mathrm{e}}}^{\mathrm{aero}}, \tag{A.8}$$

respectively, where $\boldsymbol{e}_{z_{\mathrm{i}}}$ and $\boldsymbol{e}_{y_{\mathrm{i}}}$ are the unit vectors in the direction of the z_{i} and y_{i} axes of the inertial frame.

References

Bergou, A. J., Xu, S., Wang, Z. J., oct 2007. Passive wing pitch reversal in insect flight. Journal of Fluid Mechanics 591, 321–337.

Bolsman, C. T., Goosen, J. F. L., van Keulen, F., dec 2009. Design overview of a resonant wing actuation mechanism for application in flapping wing MAVs. International Journal of Micro Air Vehicles 1 (4), 263–272.

Calogero, J. P., Frecker, M. I., Hasnain, Z., Hubbard, J. E., oct 2016. A dynamic spar numerical model for passive shape change. Smart Materials and Structures 25 (10), 104006.

Chen, Y., Skote, M., Zhao, Y., Huang, W., jul 2013. Dragonfly (Sympetrum flaveolum) flight: Kinematic measurement and modelling. Journal of Fluids and Structures 40, 115–126.

Dai, H., Luo, H., Doyle, J. F., feb 2012. Dynamic pitching of an elastic rectangular wing in hovering motion. Journal of Fluid Mechanics 693, 473–499.

de Croon, G. C. H. E., de Clercq, K. M. E., Ruijsink, R., Remes, B., de Wagter, C., 2009. Design, aerodynamics, and vision-based control of the DelFly. International Journal of Micro Air Vehicles 1 (2), 71–98.

Deng, S., Percin, M., van Oudheusden, B., feb 2016. Experimental Investigation of Aerodynamics of Flapping-Wing Micro-Air-Vehicle by Force and Flow-Field Measurements. AIAA Journal 54 (2), 1–15.

Du, G., Sun, M., jul 2008. Effects of unsteady deformation of flapping wing on its aerodynamic forces. Applied Mathematics and Mechanics 29 (6), 731–743.

Du, G., Sun, M., jul 2010. Effects of wing deformation on aerodynamic forces in hovering hoverflies. The Journal of experimental biology 213 (Pt 13), 2273–83.

Dudley, R., 2002. The biomechanics of insect flight: form, function, evolution. Princeton University Press.

Ennos, A. R., 1989. The kinematics and aerodynamics of the free flight of some diptera. Journal of Experimental Biology 142, 49–85.

Han, R., Zhang, J., Cao, L., Lu, X. Y., 2015. Propulsive performance of a passively flapping plate in a uniform flow. Journal of Hydrodynamics 27 (4), 496–501.

Howell, L. L., 2001. Compliant mechanisms. John Wiley & Sons.

Lau, G. K., Chin, Y. W., Goh, J. T. W., Wood, R. J., 2014. Dipteran-Insect-Inspired Thoracic Mechanism With Nonlinear Stiffness to Save Inertial Power of Flapping-Wing Flight. IEEE TRANSACTIONS ON ROBOTICS, 1–11.

Ma, K. Y., Chirarattananon, P., Fuller, S. B., Wood, R. J., may 2013. Controlled flight of a biologically inspired, insect-scale robot. Science 340 (6132), 603–607.

Nakata, T., Liu, H., feb 2012a. A fluidstructure interaction model of insect flight with flexible wings. Journal of Computational Physics 231 (4), 1822–1847.

Nakata, T., Liu, H., mar 2012b. Aerodynamic performance of a hovering hawkmoth with flexible wings: a computational approach. Proceedings. Biological sciences / The Royal Society 279 (1729), 722–31.

Nan, Y., Karásek, M., Lalami, M., Preumont, A., 2017. Experimental optimization of wing shape for a Hummingbird-like flapping wing Micro Air Vehicle. Bioinspiration & Biomimetics 12 (2), 026010.

Nguyen, A. T., Han, J.-H., apr 2016. Effects of fluid-structure interaction on the aerodynamics of an insect wing. In: Martín-Palma, R. J., Lakhtakia, A., Knez, M. (Eds.), Proc. SPIE 9797, Bioinspiration, Biomimetics, and Bioreplication 2016. International Society for Optics and Photonics, Las Vegas, Nevada, p. 979710.

Osborne, M. F. M., 1951. Aerodynamics of flapping flight with application to insects. Journal of Experimental Biology 28, 221–245.

Peters, H., Wang, Q., Goosen, H., van Keulen, F., 2017. Active Control of the Hinge of a Flapping Wing with Electrostatic Sticking to Modify the Passive Pitching Motion. In: Araujo, A., Soares, C. (Eds.), Volume 43 of the series Computational Methods in Applied Sciences. Springer International Publishing Switzerland 2017, pp. 153–174.

Schwab, A. L., Meijaard, J. P., 2006. How to draw Euler angles and utilize Euler parameters. In: Proceedings of IDETC/CIE ASME 2006 International Design Engineering Technical Conferences & Computers and Information in Engineering Conference. Philadelphia, Pennsylvania, USA, pp. 1–7.

Shyy, W., Lian, Y., Chimakurthi, S. K., Tang, J., Cesnik, C. E. S., Stanford, B., Ifju, P. G., 2010. Flexible wings and fluid-structure interactions for micro-air vehicles. In: Flying Insects and Robots. Springer Berlin Heidelberg, Berlin, Heidelberg, pp. 143–157.

Tanaka, H., 2012. Flexible wing structures of simplified insect-sized flapping MAVs. In: Proceedings of 2012ICME International Conference on Complex Medical Engineering. Kobe, Japa, pp. 397–401.

Tanaka, H., Wood, R. J., jul 2010. Fabrication of corrugated artificial insect wings using laser micromachined molds. Journal of Micromechanics and Microengineering 20 (7), 075008.

Trahair, N. S., jul 2005. Nonlinear Elastic Nonuniform Torsion. Journal of Structural Engineering 131 (7), 1135–1142.

Wang, Q., Goosen, J. F. L., van Keulen, F., 2014. Study of design parameters of flapping-wings. In: International Micro Air Vehicle Conference and Flight Competition (IMAV2014). Delft, The Netherlands.

Wang, Q., Goosen, J. F. L., van Keulen, F., aug 2016. A predictive quasi-steady model of aerodynamic loads on flapping wings. Journal of Fluid Mechanics 800, 688–719.

Whitney, J. P., Wood, R. J., jul 2010. Aeromechanics of passive rotation in flapping flight. Journal of Fluid Mechanics 660, 197–220.

Willmott, A. P., Ellington, C. P., nov 1997a. The mechanics of flight in the hawkmoth Manduca sexta. I. Kinematics of hovering and forward flight. The Journal of experimental biology 200 (21), 2705–2722.

Willmott, A. P., Ellington, C. P., nov 1997b. The mechanics of flight in the hawkmoth Manduca sexta. II. Aerodynamic consequences of kinematic and morphological variation. Journal of Experimental Biology 200 (21), 2723–2745.

Wootton, R. J., aug 1981. Support and deformability in insect wings. Journal of Zoology 193 (4), 447–468.

Zheng, L., Hedrick, T. L., Mittal, R., jan 2013. Time-varying wing-twist improves aerodynamic efficiency of forward flight in butterflies. PloS one 8 (1), e53060.